Journal of Computational Physics 479 (2023) 112013

Contents lists available at ScienceDirect

Journal of Computational Physics

journal homepage: www.elsevier.com/locate/jcp

Scalable matrix-free solver for 3D transfer of polarized radiation in stellar atmospheres

Pietro Benedusi [a,b,*], Simone Riva [b,c], Patrick Zulian [b], Jiří Štěpán [d], Luca Belluzzi [c,e,b,1], Rolf Krause [b,f,1]

[a] Simula Research Laboratory, Oslo, Norway
[b] Euler Institute, Università della Svizzera italiana (USI), Lugano, Switzerland
[c] Istituto Ricerche Solari "Aldo e Cele Daccò" (IRSOL), Locarno-Monti, Switzerland
[d] Astronomical Institute of the Czech Academy of Sciences, Ondřejov, Czech Republic
[e] Leibniz-Institut für Sonnenphysik (KIS), Freiburg i. Br., Germany
[f] Faculty of Mathematics and Informatics, FernUni, Brig, Switzerland

ARTICLE INFO

Article history:
Received 9 September 2022
Received in revised form 1 February 2023
Accepted 10 February 2023
Available online 20 February 2023

Keywords:
Radiative transfer
Polarization
Scattering
Krylov methods
Matrix-free
Parallel computing

ABSTRACT

We present an efficient and massively parallel solution strategy for the transfer problem of polarized radiation, for a 3D stationary medium out of local thermodynamic equilibrium. Scattering processes are included accounting for partial frequency redistribution effects. Such a setting is one of the most challenging ones in radiative transfer modeling. The problem is formulated for a two-level atomic model, which allows linearization. The discrete ordinate method alongside an exponential integrator are used for discretization. Efficient solution is obtained with a Krylov method equipped with a tailored physics-based preconditioner. A matrix-free approach results in a lightweight implementation, suited for tackling large problems. Near-optimal strong and weak scalability are obtained with two complementary decompositions of the computational domain. The presented approach made it possible to perform simulations for the Ca I line at 4227 Å with more than 10^9 degrees of freedom in less than half an hour on massively parallel machines, always converging in a few iterations for the proposed tests.

1. Introduction

Modeling the propagation of radiation in a given medium is a key task in many scientific fields, such as astrophysics [1–3], heat transfer [4], and climate science [5]. This gives rise to a large class of problems, commonly referred to as radiative transfer (RT) problems, which in general can only be solved numerically. In the astrophysical context, the numerical solution of the RT problem is a key element to interpret the information encoded in the electromagnetic radiation collected by telescopes [3]. The present work focuses on an RT problem for polarized radiation that is of high interest in solar physics research.

Currently, one of the main goals in solar physics is to improve our understanding of the magnetism in the upper layers of the solar atmosphere (the chromosphere and the transition region).[2] Indeed, the magnetic field present in these regions

* Corresponding author at: Simula Research Laboratory, Oslo, Norway.
E-mail address: benedp@usi.ch (P. Benedusi).

[1] Luca Belluzzi and Rolf Krause must be considered as equal last authors as coordinators of the project.

[2] NASA's *Heliophysics Roadmap 2014-2033* (https://science.nasa.gov/science-pink/s3fs-public/atoms/files/2014_HelioRoadmap_Final_Reduced.pdf).

https://doi.org/10.1016/j.jcp.2023.112013

plays a key role in various phenomena of high interest (e.g., coronal heating, flares, coronal mass ejections), but our knowledge of its intensity and orientation is still largely unsatisfactory. The magnetic fields in the solar atmosphere (as well as in any other astrophysical object) can be investigated by modeling the fingerprints that they leave in the polarization of the emitted radiation through a series of physical mechanisms. Unfortunately, the diagnostic methods based on the polarization signals produced by the well-known Zeeman effect, which are successfully applied at the photospheric level, are of reduced utility in the outer solar atmosphere [6]. On the other hand, during the last decades, it has been shown that the linear polarization signals produced by the scattering of anisotropic radiation in several strong resonance lines of the solar spectrum, such as H I Ly-α, Mg II k, Ca II K, Ca I 4227 Å, or Na I D_2, are sensitive to the elusive magnetic fields of the chromosphere [6,7]. Such signals presently represent one of the most promising tools to investigate the magnetic and geometrical properties of this region [8,9], and strong efforts are today devoted to their observation [10,11] and theoretical modeling [12–16].

The scattering polarization signals of strong resonance lines are primarily produced by scattering processes that are coherent in frequency in the atomic reference frame, and subject to Doppler redistribution in the observer's frame. To correctly model these signals it is essential to solve the RT problem for polarized radiation without assuming local thermodynamic equilibrium (i.e. in non-LTE conditions), and taking partial frequency redistribution (PRD) effects (i.e. correlations between the frequencies of the incoming and outgoing radiation in scattering processes) into account [17–20]. A convenient way to model PRD effects is through the redistribution matrix formalism [21–23]. In the observer's frame, the Doppler redistribution induces a complex coupling between the frequencies and propagation directions of the incident and scattered radiation, and simplifying approximations for the redistribution matrix, such as the angle-average one [21,24,22], are frequently used. However, when scattering polarization is considered, given the crucial role played by the anisotropy of the radiation field and by the geometry of the problem, such approximation can induce relevant (and not easily quantifiable) inaccuracies [25,26,16], nullifying the effort of taking the three-dimensional (3D) structure of the solar atmosphere into account. In this work, we thus consider the exact, *angle-dependent* (AD) expression of the redistribution matrix. We refer to [27] for a Fourier decomposition technique in the context of multidimensional RT modeling of scattering polarization with AD PRD.

In non-LTE conditions, the quantum state of the atoms throughout the medium is non-locally coupled via the radiation field, whose properties are themselves affected by the atomic state. Due to this coupling, the problem is in general nonlocal and nonlinear. Moreover, modeling PRD effects, considering the exact AD expression of the redistribution matrix, requires taking into account the detailed angular and frequency dependencies of the radiation field, which has to be fully stored at each spatial point, making the problem highly demanding in terms of memory, especially in 3D applications. Overall, solving numerically the discretized RT problem for polarized radiation, within a heterogeneous medium in non-LTE, and taking AD PRD effects into account, is a non-local vectorial problem in high dimensions (up to seven for the non-stationary 3D case), with high memory requirements. Such an ambitious problem requires the development and application of scalable and efficient computational strategies and the use of last generation supercomputers, as in [28,14,29].

In this work, we consider a two-level atomic model and we introduce a convenient physical assumption that allows linearization. We present an efficient solution strategy, employing a matrix-free Krylov solver coupled with tailored preconditioning and a novel parallelization strategy to ensure scalability. The presented numerical strategy and its parallel implementation make it possible to get fast and accurate solutions and to handle the high memory requirements of the problem, which would be nearly unfeasible with previous techniques. By applying these tools, we present, for the first time in the literature, illustrative numerical experiments of non-LTE RT calculations of scattering polarization with AD PRD effects, carried out in a heterogeneous 3D atmospheric model.

The article is organized as follows: in Section 2 the polarized RT problem is introduced and described. In Section 3 we present the discretization setting, followed in Section 4 by a convenient algebraic formulation of the discrete RT problem. In Section 5 we describe the parallel solution strategy and its implementation. In Section 6 numerical experiments are reported. Finally, Section 7 provides remarks and conclusions.

2. The radiative transfer problem for polarized radiation

The intensity and polarization of a beam of radiation are fully described by the four Stokes parameters, $I, Q, U, V \in \mathbb{R}$, with the intensity I being non-negative[3] and the polarization being encoded by Q, U, and V [30]. The Stokes parameters can be combined in the four-component Stokes vector

$$\boldsymbol{I} = (I, Q, U, V)^T = (I_1, I_2, I_3, I_4)^T .$$

The Stokes parameters, as well as the other physical quantities entering the problem, are in general functions of the frequency and propagation direction of the considered beam, as well as of the spatial point and time. In this work, we assume that all quantities are independent of time (stationary conditions). This is a common assumption in the astrophysical context, unless highly dynamic phenomena, like, for instance, solar and stellar flares, are considered [31].

When a beam of radiation propagates in a medium, such as the plasma of a stellar atmosphere, its intensity and polarization get modified as a result of the interaction with the particles present therein, and the possible presence of external

[3] The inequality $Q^2 + U^2 + V^2 \leq I^2$ holds.

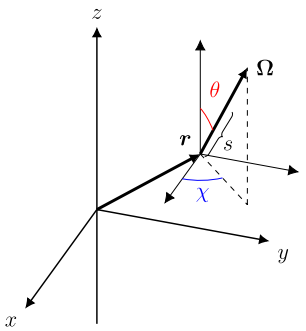

Fig. 1. We consider a right-handed Cartesian reference system with the z-axis directed along the vertical, corresponding to the radial direction in a stellar atmosphere. The position vector $\boldsymbol{r}$ is specified by its Cartesian coordinates $(x, y, z) \in D$. The unit vector $\boldsymbol{\Omega}$ is specified by its spherical coordinates: the inclination $\theta \in [0, \pi]$ measured with respect to the vertical, and the azimuth $\chi \in [0, 2\pi)$, measured on the $x - y$ plane, counter-clockwise (for an observer at $z > 0$) from the x-axis. The one-dimensional spatial coordinate along the propagation direction $\boldsymbol{\Omega}$ is denoted by s and $\boldsymbol{\Omega} \cdot \nabla \boldsymbol{I} = \mathrm{d}\boldsymbol{I}/\mathrm{d}s$.

magnetic and/or electric fields. This modification is described by the transfer equation for polarized radiation, which is integro-differential by nature. Given a domain $D \subset \mathbb{R}^3$, the RT equation for a beam of polarized radiation propagating along the unit vector $\boldsymbol{\Omega} = (\theta, \chi) \in [0, \pi] \times [0, 2\pi)$ can be written as

$$\boldsymbol{\Omega} \cdot \nabla \boldsymbol{I}(\boldsymbol{r}, \boldsymbol{\Omega}, \nu) = -K(\boldsymbol{r}, \boldsymbol{\Omega}, \nu)\boldsymbol{I}(\boldsymbol{r}, \boldsymbol{\Omega}, \nu) + \boldsymbol{\varepsilon}(\boldsymbol{r}, \boldsymbol{\Omega}, \nu), \tag{1}$$

where $\boldsymbol{r} = (x, y, z) \in D$ denotes the spatial point and $\nu \in \mathbb{R}_+$ the frequency. The coordinate system considered in this work is illustrated in Fig. 1. Equation (1) is equipped with suitable boundary conditions on ∂D, and describes a set of coupled initial values problems: non-homogeneous systems of first order ODEs of size four. The elements of the propagation matrix

$$K = \begin{pmatrix} \eta_1 & \eta_2 & \eta_3 & \eta_4 \\ \eta_2 & \eta_1 & \rho_4 & -\rho_3 \\ \eta_3 & -\rho_4 & \eta_1 & \rho_2 \\ \eta_4 & \rho_3 & -\rho_2 & \eta_1 \end{pmatrix} \in \mathbb{R}^{4\times 4},$$

describe the phenomena of absorption (η_1), dichroism (η_2, η_3, and η_4), and anomalous dispersion (ρ_2, ρ_3, and ρ_4). The four-component vector

$$\boldsymbol{\varepsilon} = (\varepsilon_1, \varepsilon_2, \varepsilon_3, \varepsilon_4)^T \in \mathbb{R}^4$$

describes the radiation emitted by the medium in the four Stokes parameters. More details on the physical meaning of K and $\boldsymbol{\varepsilon}$ can be found, for instance, in [30].

The propagation matrix K and the emission vector $\boldsymbol{\varepsilon}$ receive contributions from two types of physical processes characterizing the interaction between matter and radiation: line processes (i.e. transitions between bound states of a given atom or molecule) and continuum processes (i.e, transitions between bound and free states or between free states). The former give rise to the spectral lines, while the latter occur on a spectral range much broader than the immediate vicinity of the line resonant frequency. The contributions from line and continuum processes (hereafter labelled with the apices ℓ and c) simply add to each other.

2.1. Line processes

The line contributions to the elements of K and $\boldsymbol{\varepsilon}$ depend on the excitation state of the atom or molecule giving rise to the spectral line of interest. In general, this state has to be determined by solving a set of rate equations (statistical equilibrium equations), which describe the interaction of the atom (or molecule) with the radiation field (radiative processes), the other particles present in the medium (collisional processes), and the possible presence of external magnetic and/or electric fields.

In this work, we consider an atomic model composed of two energy levels (two-level atom). Moreover, we assume that the lower level is infinitely sharp and unpolarized. These are generally suitable assumptions when the lower level is either the ground level or a metastable level of the considered atom [30]. The explicit expression of the line contribution to the elements of the propagation matrix (η_i^ℓ and ρ_i^ℓ) for this atomic model can be found in [30, Sect. 7.2 and Appendix A13]. In addition, we neglect the role of stimulated emission; this approximation is fairly good for strong resonant lines at the shorter-wavelength part of the spectrum.

For the considered atomic model, the statistical equilibrium equations have an analytic solution, and the emission vector can be directly related to the radiation field that illuminates the atom. More precisely, the line contribution to the emission vector can be expressed as the sum of two terms:

$$\boldsymbol{\varepsilon}^{\ell}(\boldsymbol{r},\boldsymbol{\Omega},\nu)=\boldsymbol{\varepsilon}^{\ell,\mathrm{sc}}(\boldsymbol{r},\boldsymbol{\Omega},\nu)+\boldsymbol{\varepsilon}^{\ell,\mathrm{th}}(\boldsymbol{r},\boldsymbol{\Omega},\nu), \tag{2}$$

where the first one describes the contribution from radiatively excited atoms (scattering term), and the second one the contribution from atoms excited by inelastic collisions (collisional or thermal term). Using the redistribution matrix formalism, the scattering term $\boldsymbol{\varepsilon}^{\ell,\mathrm{sc}}$ is given by the following integral operator (scattering integral)

$$\boldsymbol{\varepsilon}^{\ell,\mathrm{sc}}(\boldsymbol{r},\boldsymbol{\Omega},\nu)=k_L(\boldsymbol{r})\int_{\mathbb{R}_+}\mathrm{d}\nu'\oint\frac{\mathrm{d}\boldsymbol{\Omega}'}{4\pi}R(\boldsymbol{r},\boldsymbol{\Omega}',\boldsymbol{\Omega},\nu',\nu)\,\boldsymbol{I}(\boldsymbol{r},\boldsymbol{\Omega}',\nu'), \tag{3}$$

where the convention that primed and unprimed quantities refer to the incident and scattered radiation, respectively, is used. The quantity k_L is the frequency-integrated line absorption coefficient, which is proportional to the population of the lower level. The redistribution matrix $R\in\mathbb{R}^{4\times4}$ couples, in general, all Stokes parameters, all directions, and all frequencies at each spatial point. In practice, the integral over frequencies is evaluated on an appropriate finite frequency interval $[\nu_{\min},\nu_{\max}]$.

The thermal term $\boldsymbol{\varepsilon}^{\ell,\mathrm{th}}$ does not directly depend on the radiation field. Its explicit expression for the considered two-level atomic model, under the hypothesis (always assumed in this work) of isotropic collisions can be found in [32].

2.1.1. The redistribution matrix and PRD effects

We consider the redistribution matrix for a two-level atom with an unpolarized and infinitely-sharp lower level derived by [22]. This is given by the sum of two terms:

$$R(\boldsymbol{r},\boldsymbol{\Omega}',\boldsymbol{\Omega},\nu',\nu)=R^{\mathrm{II}}(\boldsymbol{r},\boldsymbol{\Omega}',\boldsymbol{\Omega},\nu',\nu)+R^{\mathrm{III}}(\boldsymbol{r},\boldsymbol{\Omega}',\boldsymbol{\Omega},\nu',\nu)\,, \tag{4}$$

where R^{II} characterizes scattering processes that are coherent in frequency in the atomic frame (i.e. a reference frame in which the atom is at rest), and R^{III} characterizes scattering processes that are totally incoherent in the same reference frame. These terms contain the branching ratio for the scattering contribution to the emissivity (quantified by the balance between inelastic collisions and spontaneous emission) as well as the branching ratio between coherent and incoherent scattering (quantified by the balance between elastic collisions and spontaneous emission). The sum of R^{II} and R^{III} thus accounts for the relaxation of the coherence of scattering in the atomic frame due to elastic collisions.

By following a standard procedure (e.g., [21,33]), the redistribution matrix can be transformed from the atomic frame into the observer's frame, taking into account the Doppler effect due to the atomic motions. Both thermal motions, which we assume to be described by a Maxwellian distribution, and bulk motions are taken into account. The Doppler effect gives rise to further PRD phenomena in the observer's frame and induces a complex coupling between frequencies and directions in both R^{II} and R^{III}. In this work, we consider the exact angle-dependent expression of R^{II} in the observer's frame. In contrast, for R^{III} we consider the approximation of complete frequency redistribution (CRD) in the observer's frame, see [32], thanks to which the angular and frequency dependencies can be decoupled.

Using the formalism of irreducible spherical tensors for polarimetry [30, Sect. 5.11], the redistribution matrices in the observer's frame can be written as

$$R^{\mathrm{II}}(\boldsymbol{r},\boldsymbol{\Omega},\boldsymbol{\Omega}',\nu,\nu')=\sum_{KK'Q}\mathcal{R}_Q^{\mathrm{II},KK'}(\boldsymbol{r},\boldsymbol{\Omega},\boldsymbol{\Omega}',\nu,\nu')\,\mathcal{P}_Q^{KK'}(\boldsymbol{r},\boldsymbol{\Omega},\boldsymbol{\Omega}')\,, \tag{5}$$

$$R^{\mathrm{III-CRD}}(\boldsymbol{r},\boldsymbol{\Omega},\boldsymbol{\Omega}',\nu,\nu')=\sum_{KK'Q}\mathcal{R}_Q^{\mathrm{III-CRD},KK'}(\boldsymbol{r},\nu,\nu')\,\mathcal{P}_Q^{KK'}(\boldsymbol{r},\boldsymbol{\Omega},\boldsymbol{\Omega}')\,. \tag{6}$$

The explicit expression of the complex functions $\mathcal{R}_Q^{\mathrm{II},KK'}$, $\mathcal{R}_Q^{\mathrm{III-CRD},KK'}$ and of the scattering phase matrices $\mathcal{P}_Q^{KK'}\in\mathbb{C}^{4\times4}$ can be found in [32]. The computational complexity of evaluating these quantities as well as the calculation strategy used in this work are discussed in Section 3.5. Due to the complex coupling between frequencies and propagation directions in R^{II} (in its general AD form), solving the RT problem taking this redistribution matrix into account is notoriously challenging from the computational point of view. On the other hand, the PRD effects described by this matrix play a crucial role in shaping the scattering polarization profiles of strong spectral lines.

2.1.2. The CRD limit

Under certain conditions, namely when elastic collisions are very efficient and completely relax the coherence of scattering, or when the radiation field is spectrally flat, scattering processes can be suitably described as a temporal succession of independent absorption and re-emission processes [34]. This is the so-called limit of complete frequency redistribution (CRD) in which no correlation is present between the incident and scattered radiation. A solid CRD theory for the generation and transfer of polarized radiation, valid under the *flat-spectrum* assumption, is the one described in [30]. From the physical point of view, the CRD limit represents an excellent approximation for modeling weak photospheric lines, such as the Sr I line at 4607 Å [35], and a good one for modeling the Doppler core of strong chromospheric lines, such as H I Ly-α at 1215 Å [13]. From the computational and storage point of view, the limit of CRD represents a lightweight description of scattering processes, and it can be suitably applied as a preconditioner in the solution of the RT problem with PRD effects [36]. In fact,

in this limit, the incident and scattered radiation are completely decoupled, and the evaluation of the scattering integral (3) is considerably simpler than in the case of R^{II}. The explicit expression of the scattering term in the limit of CRD, for the considered atomic model, can be found in [30, Sect. 10.6].

2.2. Continuum processes

Continuum processes contribute to the emission vector through a scattering term and a thermal term, formally analogous to those brought by line processes:

$$\boldsymbol{\varepsilon}^{c}(\boldsymbol{r}, \boldsymbol{\Omega}, \nu) = \boldsymbol{\varepsilon}^{c,\text{sc}}(\boldsymbol{r}, \boldsymbol{\Omega}, \nu) + \boldsymbol{\varepsilon}^{c,\text{th}}(\boldsymbol{r}, \boldsymbol{\Omega}, \nu). \tag{7}$$

The scattering terms $\varepsilon_i^{c,\text{sc}}$ can be written in the integral form (3), by introducing a suitable redistribution matrix R^c. An explicit representation of R^c, under the assumption (considered also in this work) that continuum scattering processes are coherent in frequency in the observer's frame, can be found in [32]. Concerning $\boldsymbol{\varepsilon}^{c,\text{th}}$, it is generally a good approximation to assume that this term is isotropic and only contributes to the intensity ($\varepsilon_i^{c,\text{th}} = \varepsilon_1^{c,\text{th}}(\boldsymbol{r}, \nu)\delta_{i1}$). Regarding the propagation matrix K, under the conditions typically found in the solar atmosphere, continuum processes only contribute to the diagonal element with an isotropic term (i.e. $\eta_i^c = \eta_1^c(\boldsymbol{r}, \nu)\delta_{i1}$ and $\rho_i^c = 0$). The quantities $\varepsilon_1^{c,\text{th}}$ and η_1^c, as well as the continuum opacity for scattering σ (which appears in the expression of R^c) can be calculated with publicly available routines [e.g., 37]. Hereafter we assume that they are known a priori.

2.3. Linearization

Adding line (2) and continuum (7) contributions, the emission vector is given by

$$\begin{aligned}\boldsymbol{\varepsilon}(\boldsymbol{r}, \boldsymbol{\Omega}, \nu) &= \boldsymbol{\varepsilon}^{\ell}(\boldsymbol{r}, \boldsymbol{\Omega}, \nu) + \boldsymbol{\varepsilon}^{c}(\boldsymbol{r}, \boldsymbol{\Omega}, \nu) \\ &= \boldsymbol{\varepsilon}^{\ell,\text{sc}}(\boldsymbol{r}, \boldsymbol{\Omega}, \nu) + \boldsymbol{\varepsilon}^{\ell,\text{th}}(\boldsymbol{r}, \boldsymbol{\Omega}, \nu) + \boldsymbol{\varepsilon}^{c,\text{sc}}(\boldsymbol{r}, \boldsymbol{\Omega}, \nu) + \boldsymbol{\varepsilon}^{c,\text{th}}(\boldsymbol{r}, \nu).\end{aligned}$$

Observing that both scattering terms explicitly depend on $\boldsymbol{I}$ through a scattering integral of the form of (3), and that both thermal terms do not explicitly depend on $\boldsymbol{I}$, from a computational point of view it is convenient to group the various terms as follows

$$\boldsymbol{\varepsilon}(\boldsymbol{r}, \boldsymbol{\Omega}, \nu) = \boldsymbol{\varepsilon}^{\text{sc}}(\boldsymbol{r}, \boldsymbol{\Omega}, \nu) + \boldsymbol{\varepsilon}^{\text{th}}(\boldsymbol{r}, \boldsymbol{\Omega}, \nu), \tag{8}$$

where each term in the right-hand side contains both line and continuum contributions, e.g. $\boldsymbol{\varepsilon}^{\text{sc}} = \boldsymbol{\varepsilon}^{\ell,\text{sc}} + \boldsymbol{\varepsilon}^{c,\text{sc}}$.

It should be noted that the dependence of $\boldsymbol{\varepsilon}$ on $\boldsymbol{I}$ is not limited to the scattering integrals. Indeed, the line contributions to $\boldsymbol{\varepsilon}$ (both $\boldsymbol{\varepsilon}^{\ell,\text{sc}}$ and $\boldsymbol{\varepsilon}^{\ell,\text{th}}$) and K are all proportional, through k_L, to the population of the lower term, which in turn depends on $\boldsymbol{I}$ in a nonlinear way through the statistical equilibrium equations. A way to linearize the problem with respect to $\boldsymbol{I}$ is to fix a priori the population of the lower level, and therefore the coefficient k_L. By so doing, K and $\boldsymbol{\varepsilon}^{\ell,\text{th}}$ become independent of $\boldsymbol{I}$ and can be calculated from the atmospheric model, while $\boldsymbol{\varepsilon}$ depends on $\boldsymbol{I}$ only through the scattering integrals. Under this assumption, whose suitability was discussed in previous works [e.g., 32,38,39], the whole RT problem thus consists in the system of linear ODEs (1) linearly coupled through the integrals (3) of the scattering contributions.

The population of the lower level is taken either from the considered atmospheric model (if provided) or from independent RT calculations. The latter can be performed with available RT codes for multi-level atoms, which possibly disregard polarization (this is expected to have little impact on the population of ground or metastable levels) but include other bound-bound and bound-free transitions (e.g., ionization). In this way, accurate values of the lower level population can be used, and various spectral lines of diagnostic interest can be suitably modeled, in spite of the simplicity of the considered atomic system [19,12,16,15].

2.4. Atmospheric model and boundary conditions

We consider a cuboid domain $D = (x_{\min}, x_{\max}) \times (y_{\min}, y_{\max}) \times (z_{\min}, z_{\max})$. The radiation entering the cuboid from the top and bottom boundary faces is prescribed for all (x, y):]

$$\boldsymbol{I}(x, y, z_{\min}, \theta, \chi, \nu) = \boldsymbol{I}_{\text{in}} \qquad \text{for} \quad \theta \in [0, \pi/2), \forall\chi, \forall\nu, \tag{9}$$

$$\boldsymbol{I}(x, y, z_{\max}, \theta, \chi, \nu) = \boldsymbol{0} \qquad \text{for} \quad \theta \in (\pi/2, \pi], \forall\chi, \forall\nu, \tag{10}$$

meaning that no radiation is entering D from outer space. For the bottom boundary face, we consider an isotropic, spectrally-flat, and unpolarized incident radiation $\boldsymbol{I}_{\text{in}} = [B(x, y, z_{\min}), 0, 0, 0]^T$, where

$$B(x, y, z) = \frac{2h\nu_0^3}{c^2} \frac{1}{\exp\frac{h\nu_0}{k_B T} - 1}$$

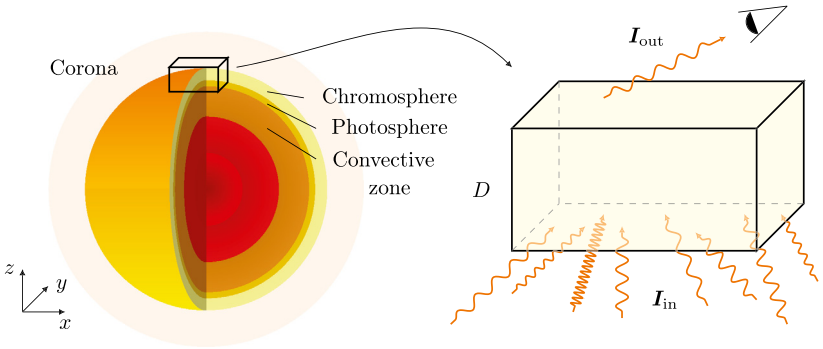

Fig. 2. Representation of the problem setting: the spatial domain D is a cuboid portion of the solar atmosphere (not in scale). The boundary data $\boldsymbol{I}_{\text{in}}$ consists in the incident radiation in $z_{\min}$. Emerging radiation $\boldsymbol{I}_{\text{out}}$ from $z_{\max}$ is observed for a particular direction and frequency. Periodic boundary conditions are enforced for $x \in \{x_{\min}, x_{\max}\}$ and $y \in \{y_{\min}, y_{\max}\}$, i.e. on the vertical faces of the domain D.

is the Planck function with ν_0 the line-center frequency, h the Planck constant, c the speed of light, and $T = T(x, y, z)$ the effective temperature. This boundary condition is suitable for atmospheric models that are semi-infinite in the vertical direction (e.g., the chromosphere), and the medium reaches thermodynamic equilibrium at its lower boundary. On the remaining boundary faces, periodic boundary conditions are imposed for all z and for all rays $(\boldsymbol{\Omega}, \nu)$:

$$\boldsymbol{I}(x_{\min}, y, z, \boldsymbol{\Omega}, \nu) = \boldsymbol{I}(x_{\max}, y, z, \boldsymbol{\Omega}, \nu),$$
$$\boldsymbol{I}(x, y_{\min}, z, \boldsymbol{\Omega}, \nu) = \boldsymbol{I}(x, y_{\max}, z, \boldsymbol{\Omega}, \nu).$$

We remark that the main quantity of interest is the radiation emergent from the upper boundary of the solar atmosphere, which we can observe from Earth, i.e. $\boldsymbol{I}(x, y, z_{\max}, \boldsymbol{\Omega}, \nu)$ for $\theta \in [0, \pi/2)$. The problem set-up is illustrated in Fig. 2.

In practice, a given atmospheric model (e.g., a model from [40], resulting from a magneto-hydrodynamic simulation of the solar atmosphere) determines the spatial domain D, fixes the discrete spatial grid, and provides a series of thermodynamic quantities (e.g., temperature, density, magnetic field vector, etc.) at each spatial point. From the atmospheric model it is possible to evaluate a-priori the redistribution matrix R and, under the assumption that the coefficient k_L is known, the propagation matrix K, and the thermal emissivity $\boldsymbol{\varepsilon}^{\text{th}}$.

3. Discretization

Depending on the particular application, the RT problem has been discretized using a variety of methods. For the angular discretization, we recall the spherical harmonics method [41], used to recover smooth solutions when scattering depends only on the scattering angle $\Theta = \arccos(\boldsymbol{\Omega} \cdot \boldsymbol{\Omega}')$ [5]. In the more general case, the discrete ordinates method (DOM), also known as S_N method, is often used [42–44]: in order to compute scattering integrals, the angular coordinates $\boldsymbol{\Omega} = (\theta, \chi)$ are discretized with appropriate angular quadrature weights, leading to a set of semi-discrete RT equations.

The angular discretization is then coupled with a discretization of the spatial variable $\boldsymbol{r}$. In this context, finite element or finite volume methods can be used to discretize (1), especially when dealing with complex geometries [45–47]. The discontinuous Galerkin (DG) method [48,49], or hybrid methods [50–53] have also been employed. For structured spatial grids, finite difference [54], Runge-Kutta [55], or the short characteristic method [56] are commonly used.

In this work, being D a cuboid, we use a DOM angular discretization coupled with an exponential integrator method in space, which are briefly described in Sections 3.1-3.3.

3.1. Angular discretization

For the angular discretization of $\boldsymbol{\Omega} = (\theta, \chi)$, we use a tensor product quadrature. For the inclination $\mu = \cos(\theta) \in [-1, 1]$, we consider two Gauss-Legendre grids (and corresponding weights) with $N_\theta/2$ nodes each, namely

$$-1 < \mu_1 < \mu_2 < \cdots < \mu_{N_\theta/2} < 0 < \mu_{N_\theta/2+1} < \cdots < \mu_{N_\theta} < 1,$$

for $\mu \in (-1, 0)$ and $\mu \in (0, 1)$, respectively. These grid nodes correspond to the angles $\theta_l = \arccos(\mu_l) \in (0, \pi)$, for $l = 1, \ldots, N_\theta$, with N_θ even. For the azimuth $\chi \in (0, 2\pi]$, we consider an equidistant grid (and corresponding trapezoidal weights) with N_χ nodes, namely

$$\chi_m = (m - 1/2) \cdot \frac{2\pi}{N_\chi} \quad \text{for} \quad m = 1, \ldots, N_\chi.$$

For notational convenience, we introduce multi-indices, so that $\boldsymbol{\Omega}_{\boldsymbol{l}} = (\theta_l, \chi_m)$ denotes the angular grid, with $\boldsymbol{l} = \mathbf{1}, \ldots, \mathbf{M}$ and $\mathbf{M} = (N_\theta, N_\chi)$, ordered with a lexicographic criterion.

3.2. Frequency discretization

The considered spectral interval $[\nu_{\min}, \nu_{\max}]$ is discretized with a unevenly spaced grid with N_ν nodes, namely

$$\nu_{\min} = \nu_1 < \nu_2 < \cdots < \nu_{N_\nu} = \nu_{\max}.$$

The frequency grid $\{\nu_n\}_{n=1}^{N_\nu}$ is usually finer in the line core (i.e. in a neighbourhood of ν_0), where the nodes are equally spaced, and coarser in the wings, where the nodes distance increases logarithmically (e.g. Section 6.2).

3.3. Spatial discretization

The spatial domain D is discretized with $N_s = N_x N_y N_z$ nodes on an unevenly spaced grid, with nodes $\mathbf{r_i} = (x_i, y_j, z_k)$ and $\boldsymbol{i} = \mathbf{1}, ..., \mathbf{N}$, using multi-indices $\boldsymbol{i} = (i, j, k)$ with $\mathbf{N} = (N_x, N_y, N_z)$ and a lexicographic ordering; taking into account periodic boundary conditions we have:

$$x_{\min} = x_1 < x_2 < \cdots < x_{N_x} < x_{\max}$$

and similarly for y. For z we have

$$z_{\min} = z_1 < z_2 < \cdots < z_{N_z} = z_{\max}.$$

Given the total number of degrees of freedom $N = 4 \cdot N_s N_\theta N_\chi N_\nu$, we consider the collocation vectors of the Stokes and emission vectors, respectively $\mathbf{I}, \boldsymbol{\epsilon} \in \mathbb{R}^N$, ordered with a lexicographic criterion, namely

$$\mathbf{I} = [\mathbf{I_1}, \mathbf{I_2}, \mathbf{I_3}, ..., \mathbf{I_N}]^T, \quad \boldsymbol{\epsilon} = [\boldsymbol{\epsilon_1}, \boldsymbol{\epsilon_2}, \boldsymbol{\epsilon_3}..., \boldsymbol{\epsilon_N}]^T, \tag{11}$$

where $\mathbf{I_i}, \boldsymbol{\epsilon_i} \in \mathbb{R}^{4N_\theta N_\chi N_\nu}$ collect all the rays in $\mathbf{r_i}$, i.e.

$$\mathbf{I_i} = [I_1(\mathbf{r_i}, \boldsymbol{\Omega_1}, \nu_1), \ldots, I_4(\mathbf{r_i}, \boldsymbol{\Omega_1}, \nu_1), I_1(\mathbf{r_i}, \boldsymbol{\Omega_1}, \nu_2), \ldots, I_3(\mathbf{r_i}, \boldsymbol{\Omega_M}, \nu_{N_\nu}), I_4(\mathbf{r_i}, \boldsymbol{\Omega_M}, \nu_{N_\nu})]^T,$$

and similarly for $\boldsymbol{\epsilon_i}$. Likewise, the vectors $\boldsymbol{\eta}, \boldsymbol{\rho} \in \mathbb{R}^N$ can be used to collect the entries of K (the unphysical component ρ_1 is formally set to zero in $\boldsymbol{\rho}$). For notational simplicity, an abuse of notation is employed: the symbols $\boldsymbol{I}$ and I are used to denote both the continuous solution of (1) and its numerical approximation.

3.4. 3D formal solution

If the propagation matrix K and the emission vector $\boldsymbol{\varepsilon}$ are known at each spatial point, the solution of the ODEs system (1) can be numerically approximated for each ray $(\boldsymbol{\Omega_l}, \nu_n)$ and spatial node $\mathbf{r_i}$ applying a suitable integrator: in the astrophysical context this process is known as *formal solution*. More compactly, the formal solution is the numerical process to obtain $\mathbf{I}$ through (1) given $\boldsymbol{\epsilon}$, the propagation matrix, and the boundary data.

A common choice for the solution of (1) are exponential integrators (a.k.a. DELO methods in the RT context) [57–59], which we briefly describe. For any ray $(\boldsymbol{\Omega}, \nu)$ and initial point $\boldsymbol{r}_0 \in D$, given K and the emissivity $\boldsymbol{\varepsilon}$, one first rewrites (1), introducing the one-dimensional local coordinate s along $\boldsymbol{\Omega}$, with $s = 0$ corresponding to $\boldsymbol{r}_0$ (cf. Fig. 1)

$$\begin{aligned} &\frac{\mathrm{d}}{\mathrm{d}s}\boldsymbol{I}(s, \boldsymbol{\Omega}, \nu) = \eta_1(s, \boldsymbol{\Omega}, \nu)[\boldsymbol{S}(s, \boldsymbol{\Omega}, \nu) - \boldsymbol{I}(s, \boldsymbol{\Omega}, \nu)], \\ &\boldsymbol{I}(0, \boldsymbol{\Omega}, \nu) = \boldsymbol{I}_0(\boldsymbol{\Omega}, \nu), \end{aligned} \tag{12}$$

where $\boldsymbol{I}_0(\boldsymbol{\Omega}, \nu) = \boldsymbol{I}(\boldsymbol{r}_0, \boldsymbol{\Omega}, \nu)$ is known either from the boundary conditions (9)-(10) or from the solution of the same equation up to $\boldsymbol{r}_0$ (propagating the ray back until the boundary is reached) and

$$\boldsymbol{S}(s, \boldsymbol{\Omega}, \nu) = \left(Id - \frac{K(s, \boldsymbol{\Omega}, \nu)}{\eta_1(s, \boldsymbol{\Omega}, \nu)}\right)\boldsymbol{I}(s, \boldsymbol{\Omega}, \nu) + \frac{\boldsymbol{\varepsilon}(s, \boldsymbol{\Omega}, \nu)}{\eta_1(s, \boldsymbol{\Omega}, \nu)}.$$

The exact integration of (12) yields to the *variation of constants* formula

$$\boldsymbol{I}(s, \boldsymbol{\Omega}, \nu) = e^{-\Delta\tau(s)}\boldsymbol{I}_0(\boldsymbol{\Omega}, \nu) - \int_0^s \mathrm{d}x\, e^{-\Delta\tau(x)}\boldsymbol{S}(x, \boldsymbol{\Omega}, \nu), \tag{13}$$

where $\Delta\tau(y) = \Delta\tau(y, \boldsymbol{\Omega}, \nu)$ is given by

$$\Delta\tau(y, \boldsymbol{\Omega}, \nu) = \int_0^y \mathrm{d}x\, \eta_1(x, \boldsymbol{\Omega}, \nu). \tag{14}$$

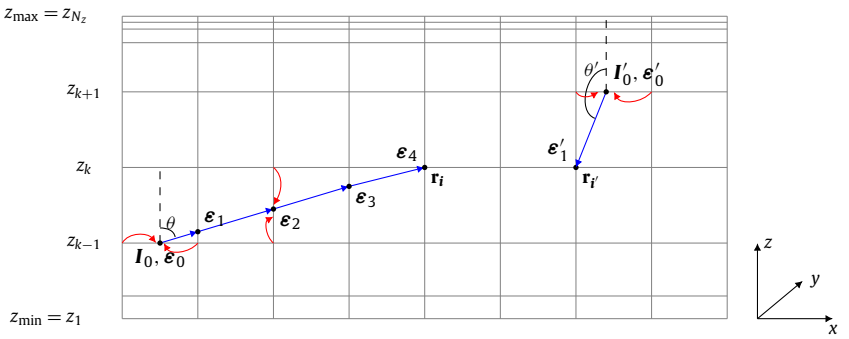

Fig. 3. Example of formal solution along two rays. For simplicity we consider a 2D setting, corresponding to $\chi = 0$ or $\chi = \pi$; the extension to the general 3D case is natural. The first ray on the left corresponds to $\theta < \pi/2$ and is used to compute $\boldsymbol{I}(\mathbf{r}_{\boldsymbol{i}}, \theta, 0, \nu)$ for any ν. In this case, we consider the ray up to z_{k-1} and $P = 5$ intersections with the grid are found. The initial condition $\boldsymbol{I}_0$ is found through linear interpolation from $\boldsymbol{I}(x_n, y_m, z_{k-1}, \theta, 0, \nu)$, which is known for all n, m. Similarly, the emission vectors $\boldsymbol{\epsilon}_p$ for $p = 0, .., 3$ can be computed by interpolating (e.g., as shown in red for $\boldsymbol{\epsilon}_0$ and $\boldsymbol{\epsilon}_2$) while $\boldsymbol{\epsilon}_4$ is known. Then, $\boldsymbol{I}(\mathbf{r}_{\boldsymbol{i}}, \theta, 0, \nu)$ is numerically computed solving four ODEs systems in sequence. The left ray illustrates a case for which $P = 2$, $\theta' > \pi/2$, $\chi = \pi$ and $\boldsymbol{i}' = (i + 2, j, k)$. A single ODEs system has to be solved in this case to obtain $\boldsymbol{I}(\mathbf{r}_{\boldsymbol{i}'}, \theta', 0, \nu)$. In both cases propagation matrices K_p are also obtained using linear interpolation. (For interpretation of the colors in the figure(s), the reader is referred to the web version of this article.)

A large variety of numerical schemes are available to approximate the integral in (13). In particular, a linear approximation of $\boldsymbol{S}$ in the integration interval produces the DELO-linear method, which is an L-stable method particularly suited for the solution of (12) since it guarantees stability, resolving exactly the exponential decay of the solution due to absorption processes. The DELO-linear method will be used in Section 6, for numerical experiments. We refer to [59–62] for a detailed review of DELO methods and their convergence and stability properties in the context of transfer of polarized radiation. It is worth mentioning that any other formal solver, e.g. high-order methods, which would be more suited for realistic applications, can be applied without altering the essence of this work. In this regard, a parabolic BESSER method [28] has been successfully tested. We finally remark that DELO methods require the spatial scale conversion from the geometrical scale to the optical depth scale described by (14); details on this conversion are given in [61]. The numerical solution of (12) is carried out at each spatial point $\mathbf{r}_{\boldsymbol{i}}$ for all the $N_\theta N_\chi N_\nu$ rays. The ordering in which the spatial domain is crossed depends on the direction $\boldsymbol{\Omega}_{\boldsymbol{l}} = (\theta_l, \chi_m)$ under consideration so that an initial condition is available. More precisely: for $\theta_l < \pi/2$ deeper layers are considered first (i.e. D is crossed from $z_{\min} = z_1$ to $z_{\max} = z_{N_z}$); the reverse ordering is used if $\theta_l > \pi/2$. A lexicographic (resp. reverse) ordering is used in x if $\cos(\chi_m) > 0$ (resp. $\cos(\chi_m) < 0$). Similarly, a lexicographic (resp. reverse) ordering is used in y if $\sin(\chi_m) > 0$ (resp. $\sin(\chi_m) < 0$).

The initial condition is obtained from the previous ($z_{k\pm1}$) atmospheric height. If more than a single grid cell is crossed by a ray, the solution is split into multiple steps and quantities outside spatial nodes are obtained through linear interpolation. Details about this geometric algorithm are reported in Algorithm 1 and illustrated in Fig. 3. Crucially, the formal solution requires $O(N) = O(N_s N_\theta N_\chi N_\nu)$ operations and consists of $N_\theta N_\chi N_\nu$ independent ODEs systems (12) for each spatial point. Its execution is well suited for an embarrassingly parallel implementation, using up to $N_\theta N_\chi N_\nu$ processors.

Algorithm 1: Perform a formal solution in 3D, i.e. compute $\mathbf{I} = \Lambda\boldsymbol{\epsilon}$, with Λ the formal solver operator.

Input: $\boldsymbol{\epsilon} \in \mathbb{R}^N$
Data: boundary data and vectors $\boldsymbol{\eta}, \boldsymbol{\rho} \in \mathbb{R}^N$ to build the propagation matrices K on demand.
for $\boldsymbol{l} = \mathbf{1}, \ldots, \boldsymbol{M}$ **do**
  Given $\boldsymbol{\Omega}_{\boldsymbol{l}} = (\theta_l, \chi_m)$, depending on $\cos(\theta_l)$, $\cos(\chi_m)$, and $\sin(\chi_m)$ signs, identify the ordering for the spatial loop over $\boldsymbol{i} = (i, j, k)$ (the loop on k being always the outer one).
  for $n = 1, \ldots, N_\nu$ **do**
    for $\boldsymbol{i} \in \{\mathbf{1}, \ldots, \mathbf{N}\}$ **do**
      Find $P \geq 2$ intersection points between the direction $\boldsymbol{\Omega}_{\boldsymbol{l}}$ at $\mathbf{r}_{\boldsymbol{i}}$ and the spatial grid up to the previous horizontal plane (corresponding to z_{k-1} or z_{k+1}), where $\boldsymbol{I}(x_s, y_q, z_{k\pm1}, \boldsymbol{\Omega}_{\boldsymbol{l}}, \nu_n)$ is known for all s, q from the previous spatial iterate or from boundary conditions.
      Using linear interpolation, for $p = 0, \ldots, P-1$ compute emission vectors $\boldsymbol{\varepsilon}_p \in \mathbb{R}^4$ (resp. matrices K_p) at the intersection points from $\boldsymbol{\epsilon}$ (resp. $\boldsymbol{\eta}, \boldsymbol{\rho}$). Similarly compute initial condition $\boldsymbol{I}_0 \in \mathbb{R}^4$ from $\boldsymbol{I}$, cf. Fig. 3.
      Numerically solve the ODEs (12) $P-1$ times (e.g. using the DELO-linear method) given $\{\boldsymbol{\varepsilon}_p\}_{p=0}^{P}$ and $\boldsymbol{I}_0$.
      Obtain $\boldsymbol{I}(\mathbf{r}_{\boldsymbol{i}}, \boldsymbol{\Omega}_{\boldsymbol{l}}, \nu_n)$.
    end
  end
end
Output: $\mathbf{I} \in \mathbb{R}^N$

3.5. Scattering integral

Recalling equations (4)-(8), the scattering contribution to the emission coefficient $\boldsymbol{\epsilon}^{\mathrm{SC}}$ can be written as

$$\boldsymbol{\epsilon}^{\mathrm{SC}} = \boldsymbol{\epsilon}^{\mathrm{SC,II}} + \boldsymbol{\epsilon}^{\mathrm{SC,III}} + \boldsymbol{\epsilon}^{\mathrm{SC},c}, \tag{15}$$

where $\boldsymbol{\epsilon}^{\mathrm{SC,II}}$ and $\boldsymbol{\epsilon}^{\mathrm{SC,III}}$ are the line contributions associated to the R^{II} and R^{III} redistribution matrices, respectively, and $\boldsymbol{\epsilon}^{\mathrm{SC},c}$ is the continuum contribution. In this section, we briefly describe the strategy devised to compute $\boldsymbol{\epsilon}^{\mathrm{SC,II}}$, which is by far the most demanding contribution in terms of computational complexity.

The quantity $\boldsymbol{\varepsilon}^{\mathrm{SC,II}}$ is calculated in a reference system in which the bulk velocity is zero (comoving system). If bulk velocities are present, their value in the observer's system is found via interpolations on the frequency axis. In this procedure, corrections to the propagation directions due to aberration and relativistic effects are neglected. When evaluating the integral in (3), we first perform the integration over the frequency ν', and then the one over the direction $\boldsymbol{\Omega}'$. The evaluation of the frequency integral presents two main difficulties: a) R^{II} exhibits a very complex behaviour as a function of ν', which is strongly influenced by the scattering angle $\Theta = \arccos(\boldsymbol{\Omega}\cdot\boldsymbol{\Omega}')$ and by the frequency ν of the emitted radiation, thus making necessary the use of a priori adapted unstructured grids; b) the computation of R^{II} implies several evaluations of the Faddeeva function, requiring iterative algorithms and considerable computational resources.

By considering the aforementioned difficulties, we developed a strategy that minimizes the number of evaluations of the Faddeeva function, which we compute using the efficient algorithm developed by S.G. Johnson.[4] In particular, we exploit the fact that the function $\mathcal{R}_{\mathrm{Q}}^{\mathrm{II},KK'}$ defined in equation (5) depends on the scattering angle Θ. If the considered angular grid is sufficiently regular, the number of different values that this angle can take, N_Θ, is much smaller than the total number of direction pairs, $N_\theta^2 N_\chi^2$. To perform the quadrature over ν', for any set of parameters $\beta = (\mathbf{r}_i, \nu_n, \Theta_p)$, we build a dedicated grid $\mathcal{G}$ of size S, which contains the quadrature nodes and weights, and the corresponding values of $\mathcal{R}_{\mathrm{Q}}^{\mathrm{II},KK'}$:

$$\mathcal{G}(\beta) = \left\{ \nu'^{\mathcal{G}}_d,\, w^{\mathcal{G}}_d,\, \left(\mathcal{R}_{\mathrm{Q}}^{\mathrm{II},KK'}\right)^{\mathcal{G}}_d \right\}_{d=1}^{S(\beta)}.$$

We point out that the quadrature nodes $\{\nu'^{\mathcal{G}}_d\}_{d=1}^{S}$ do not coincide with the nodes of the frequency grid of the problem $\{\nu_n\}_{n=1}^{N_\nu}$, and the values of the radiation field at such frequencies must be calculated through interpolations. In 3D applications, due to the large number of degrees of freedom, it is not feasible to precompute and store the grids $\mathcal{G}$ for all possible sets of parameters β. In this case, the grids $\mathcal{G}$ are therefore computed on the fly when required. Our strategy, with complexity $O(N_s N_\theta^2 N_\chi^2 N_\nu^2)$, is summarized in Algorithm 2.

Algorithm 2: Compute $\boldsymbol{\epsilon}^{\mathrm{SC,II}}$.

Input: $\mathbf{I} \in \mathbb{R}^N$,
Data: angular quadrature weights $\{w_{\boldsymbol{m}}\}_{\boldsymbol{m}=\mathbf{1}}^{\boldsymbol{M}}$, scattering angles $\{\Theta_p\}_{p=1}^{N_\Theta}$, atomic and atmospheric parameters.
for $\boldsymbol{i} = \mathbf{1}, \dots, \mathbf{N}$ **do**
  Build database for $\mathcal{G}$ in $\mathbf{r}_{\boldsymbol{i}}$ for all $\{\Theta_p\}_{p=1}^{N_\Theta}$ and $\{\nu_n\}_{n=1}^{N_\nu}$
  for $\boldsymbol{l} = \mathbf{1}, \dots, \mathbf{M}$ **do**
    for $n = 1, \dots, N_\nu$ **do**
      $\boldsymbol{\epsilon}^{\mathrm{SC,II}}(\mathbf{r}_{\boldsymbol{i}}, \boldsymbol{\Omega}_{\boldsymbol{l}}, \nu_n) = 0$
      for $\boldsymbol{m} = \mathbf{1}, \dots, \mathbf{M}$ **do**
        Find scattering angle Θ_p corresponding to pair $(\boldsymbol{\Omega}_{\boldsymbol{l}}, \boldsymbol{\Omega}'_{\boldsymbol{m}})$
        From database select grid $\mathcal{G}(\beta)$ of size $S(\beta)$, corresponding to parameters $\beta = (\mathbf{r}_{\boldsymbol{i}}, \nu_n, \Theta_p)$

$$\boldsymbol{\epsilon}^{\mathrm{SC,II}}(\mathbf{r}_{\boldsymbol{i}}, \boldsymbol{\Omega}_{\boldsymbol{l}}, \nu_n) = \boldsymbol{\epsilon}^{\mathrm{SC,II}}(\mathbf{r}_{\boldsymbol{i}}, \boldsymbol{\Omega}_{\boldsymbol{l}}, \nu_n) + w_{\boldsymbol{m}} \sum_{KK'Q} \mathcal{P}_{\mathrm{Q}}^{KK'}(\mathbf{r}_{\boldsymbol{i}}, \boldsymbol{\Omega}_{\boldsymbol{l}}, \boldsymbol{\Omega}'_{\boldsymbol{m}}) \sum_{d=1}^{S} w^{\mathcal{G}}_d \left(\mathcal{R}_{\mathrm{Q}}^{\mathrm{II},KK'}\right)^{\mathcal{G}}_d \boldsymbol{I}(\mathbf{r}_{\boldsymbol{i}}, \boldsymbol{\Omega}'_{\boldsymbol{m}}, \nu'^{\mathcal{G}}_d)$$

        end
      end
    end
  end
  Free database for $\mathcal{G}$.
end
Output: $\boldsymbol{\epsilon}^{\mathrm{SC,II}} \in \mathbb{R}^N$

As far as $\boldsymbol{\epsilon}^{\mathrm{SC,III}}$ is concerned, the approximation of CRD in the observer's frame for the R^{III} redistribution matrix (cf. Section 2.1.1) allows decoupling the dependencies on the incoming and outgoing beams. For this term, fast computational methods with $O(N_s N_\theta N_\chi N_\nu)$ complexity are therefore possible. The same applies when the limit of CRD (cf. Section 2.1.2)

[4] http://ab-initio.mit.edu/wiki/index.php/Faddeeva_Package.

is considered. Thanks to the assumption that continuum scattering processes are coherent in frequency in the observer's frame (cf. Section 2.2), also the evaluation of $\boldsymbol{\epsilon}^{c,\mathrm{sc}}$ does not present particular difficulties. Numerical experiments in Section 6 confirm that the computation of $\boldsymbol{\epsilon}^{\mathrm{sc,II}}$ is by far the most demanding step in the calculation of the emission vector in the PRD setting.

4. Algebraic formulation

A suitable algebraic formulation of the problem is a key step for the setup of an efficient solution strategy. We consider the algebraic formulation presented in [36] for the 1D case. The solution of the RT problem is divided into two components (cf. Sections 3.4-3.5): the solution of the RT equation (1) (i.e. the formal solution) and the calculation of the emissivity (8). We recall that both the initial value problem (12) and the integral (3) are linear w.r.t. $\boldsymbol{I}$ and $\boldsymbol{\varepsilon}$. Given a discrete emissivity $\boldsymbol{\epsilon}$, the solution of all discretized transfer ODEs systems in (1), i.e. the application of Algorithm 1 can be written as

$$\mathbf{I} = \Lambda\boldsymbol{\epsilon} + \mathbf{t}, \tag{16}$$

where $\Lambda : \mathbb{R}^N \to \mathbb{R}^N$ is the linear transfer operator, encoding the used numerical scheme (e.g. the DELO-linear formal solver) and the set of K matrices. The vector $\mathbf{t} \in \mathbb{R}^N$ encodes boundary conditions. The action of Λ alone can be encoded in a matrix-free form, i.e. using Algorithm 1 with zero boundary conditions. The vector $\mathbf{t}$ can be computed using Algorithm 1, setting $\boldsymbol{\epsilon} = 0$ and using the prescribed boundary conditions from (9)-(10).

Similarly, the discrete computation of the emissivity (8) can be written as

$$\boldsymbol{\epsilon} = \boldsymbol{\epsilon}^{\mathrm{sc}} + \boldsymbol{\epsilon}^{\mathrm{th}} = \Sigma\mathbf{I} + \boldsymbol{\epsilon}^{\mathrm{th}}, \tag{17}$$

where the linear operator $\Sigma : \mathbb{R}^N \to \mathbb{R}^N$, cf. Algorithm 2, encodes the discretized scattering integral (3), and depends on the numerical quadrature. Under the considered assumptions (see Section 2.3), the thermal term $\boldsymbol{\epsilon}^{\mathrm{th}}$ can be evaluated a priori from the atmospheric parameters. Using the ordering in (11) we have

$$\Sigma = \begin{pmatrix} \Sigma_{\mathbf{1}} & & & \\ & \Sigma_{\mathbf{2}} & & \\ & & \ddots & \\ & & & \Sigma_{\boldsymbol{N}} \end{pmatrix},$$

where the $\Sigma_{\boldsymbol{i}}$ blocks are dense because of the structure of R in (3). The block diagonal structure of Σ is well suited for a parallel evaluation on each spatial node, as the structure of Algorithm 2 suggests. On the other hand, the action of Λ couples different spatial nodes, but each ray $(\boldsymbol{\Omega_I}, \nu_m)$ can be evaluated independently. As for the operator Λ, also the action of Σ can be encoded in a matrix-free form to avoid storage and assembly costs. As pointed out in Sections 3.4-3.5, the application of Λ and Σ comes at different computational complexities ($O(N)$ and $O(NN_\theta N_\chi N_\nu)$ respectively).

Combining (16) and (17), we can formulate the whole discrete RT problem as a single size N linear system with unknown $\mathbf{I}$, namely

$$(Id - \Lambda\Sigma)\mathbf{I} = \Lambda\boldsymbol{\epsilon}^{\mathrm{th}} + \mathbf{t}, \tag{18}$$

where Id is the identity matrix. In realistic settings, where anisotropic and heterogeneous coefficients, as well as unevenly spaced grids, are present, $Id - \Lambda\Sigma$ is not symmetric.

5. Scalable solution strategy

The structure of the linear system (18) suggests the use of a fixed point iteration (a.k.a. Λ-iteration or source iteration), i.e. iterating between (16) and (17) until convergence. However, this iterative process converges too slowly for practical applications. Therefore, more effective strategies are employed, such as diagonal or block-diagonal[5] preconditioning [63,64, 38], diffusion based preconditioning [65], and multigrid techniques [66].

More recently, preconditioned Krylov methods gained popularity in the RT context [67–71,29,72,39]. Crucially, Krylov methods are well suited for matrix-free approaches and proved to be highly effective solution strategies for large linear systems. We refer to [36] for a study about matrix-free approaches in polarized RT and to [73] for a recent work with a semi-matrix-free setting. We recall that the explicit assembly of the dense matrix $Id - \Lambda\Sigma$ in (18) is not suitable for practical 3D applications, where typically $N > 10^9$.

[5] Diagonal or Jacobi preconditioners are also known as accelerated lambda iteration (ALI) in the astrophysical context.

5.1. Matrix-free preconditioned Krylov method

For the solution of the linear system (18), we use the matrix-free preconditioned GMRES (PGMRES) method introduced in [36]. Effective preconditioning is obtained in a physics-based framework, using $P = Id - \Lambda\widetilde{\Sigma}$ where $\widetilde{\Sigma}$ is a cheap approximation of Σ. In particular, $\widetilde{\Sigma}$ corresponds to the CRD scattering model (cf. Section 2.1.2), with highly reduced computational complexity (cf. Section 3.5). The action of P^{-1} is obtained using, again, a matrix-free GMRES method, so that the solution strategy consists of two nested GMRES iterations.[6] As shown in [36] for a 1D plane-parallel geometry, and confirmed herein for a more general setting, the proposed solution strategy is robust w.r.t. discretization parameters.

5.2. Parallel implementation

As pointed out in Sections 3-4, different algorithmic stages can be executed in parallel in different dimensions, in a mutually exclusive way. To take advantage of parallelization in each stage, two copies of the quantities of interest are stored, with different distributions among processors. A primary grid, where the radiation field $\mathbf{I}$ and all atmospheric quantities are stored, and where the scattering integral Σ is calculated, is distributed spatially, with each processor corresponding to a subdomain of D with N_s/N_p spatial grid points, where N_p is the number of processors.[7] On a second grid, where only the formal solution Λ is performed, auxiliary vectors $\mathbf{I}_a, \boldsymbol{\epsilon}_a, \boldsymbol{\eta}_a, \boldsymbol{\rho}_a \in \mathbb{R}^N$ are stored with a ray-wise distribution: each processor owns these quantities in all spatial points for a subset of rays with size $N_r = N_\theta N_\chi N_\nu / N_p$. In order to reduce memory requirements and message size in the communication, we can subdivide N_r into $\mathcal{T}$ tiles hence allocating a buffer for processing of size $(N_r/\mathcal{T})N_s$ for each MPI process. Tiles are communicated using the MPI collective `MPI_Alltoall()`. Fig. 4 illustrates the data and domain decompositions for an example with $N_p = 4$. The parallel evaluation of the operator $Id - \Lambda\Sigma$ is summarized in Algorithm 3.

In terms of memory, the auxiliary grid corresponds to a minor overhead (by a factor of ≈ 1.5) w.r.t. the primary one, at least for $N_p \leq N_\theta N_\chi N_\nu$. For larger N_p, the storage requirements of the auxiliary grid are no longer scaling and the memory overhead will increase unless the auxiliary grid is further decomposed, e.g. along the z axis.[8] We remark that for a typical RT application in a state-of-the-art 3D model of the solar atmosphere, $N_s = 500^3$ and $N_\theta N_\chi N_\nu = 10^4$, so that the storage of a single field (e.g. $\mathbf{I}$) would require $N \cdot 8$ bytes $= 40$ TB. To put this number into context, with the same grid, a two-level atom CRD simulation would approximately require 10 GB only, since significantly fewer unknowns (e.g., the nine components of the frequency-averaged radiation field tensor [30]) need to be stored at each spatial point. For this reason, parallelization techniques where the spatial domain is only decomposed on the z-axis [28] are suited for the CRD setting but completely inadequate for the AD PRD case.

We remark that parallel scheduling for structured grids [74–76] can be used to further increase the scalability of the formal solution for $N_p > N_\theta N_\chi N_\nu$. Nevertheless, in the PRD setting, the formal solution is negligible in terms of run-time (cf. scaling experiments in Section 6), as opposed to the CRD case where it is dominant.

Algorithm 3: Parallel evaluation of the RT operator $Id - \Lambda\Sigma$.

Input: $\mathbf{I} \in \mathbb{R}^N$ defined on the primary grid, spatially distributed
Data: data from Algorithms 1-2 on the primary grid. Setup: copy $\boldsymbol{\eta}, \boldsymbol{\rho}$ in the auxiliary grids and obtain $\boldsymbol{\eta}_a, \boldsymbol{\rho}_a$.
Compute $\boldsymbol{\epsilon} = \Sigma\mathbf{I}$ with Algorithm 2, in parallel on different spatial nodes.
All-to-all communication: $\boldsymbol{\epsilon} \to \boldsymbol{\epsilon}_a$, copying the emission vector on the auxiliary grids.
Compute $\mathbf{I}_a = \Lambda\boldsymbol{\epsilon}_a$ with Algorithm 1, in parallel on different rays.
All-to-all communication: $\mathbf{I}_a \to \mathbf{I}_{tmp}$, copying back the intensity vector on the primary grid.
Output: $\mathbf{I} - \mathbf{I}_{tmp} \in \mathbb{R}^N$

For the distributed algebraic operations and Krylov solver we use the C library PETSc [77–79]. For the grid management, data-redistribution, and tiling strategy we developed the open-source C++ code SGRID [80].

6. Numerical experiments

Numerical experiments have been performed on the Cray XC40 nodes of the Piz Daint supercomputer of the Swiss national supercomputing centre (CSCS).[9] The used partition features 1813 computation nodes, each of which holds two 18-core Intel Xeon E5-2695v4 (2.10GHz) processors. We use the default GMRES settings from PETSc, i.e. a zero initial guess, restart after 30 iterations, and a threshold of 10^{-5} for the preconditioned relative residual norm as a stopping criterion.

[6] This technique is also known as flexible GMRES (FGMRES), where the action of the preconditioner P^{-1} is approximated iteratively, e.g. with a second GMRES method.

[7] For simplicity, we assume both N_s and $N_\theta N_\chi N_\nu$ being divisible by N_p.

[8] Applying Λ for a spatial grid decomposed in the x, y axis is notoriously challenging since arbitrary far subdomains can be coupled, especially for rays with $\theta \approx \pi/2$.

[9] https://www.cscs.ch/computers/piz-daint/.

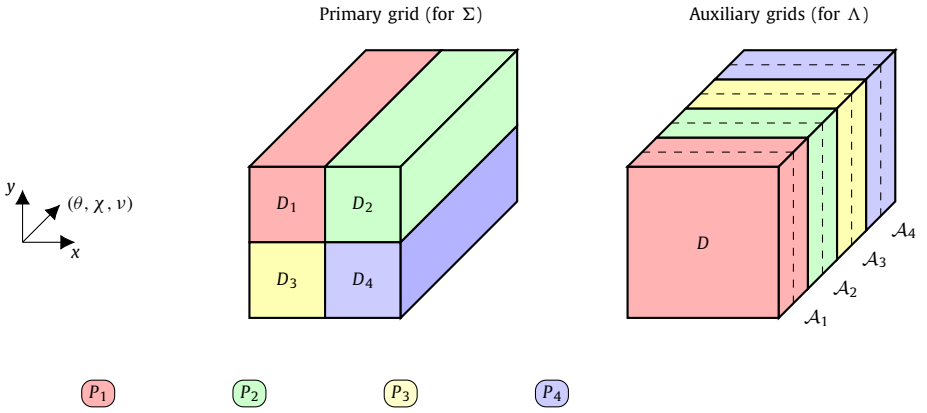

Fig. 4. Decomposition of primary and auxiliary grids for $N_p = 4$. The spatial domain is only illustrated for two spatial dimensions x and y; the third dimension is used to include different rays (θ, χ, ν). Left: domain decomposition $D = \cup_{i=1,\dots,4} D_i$. Each processor P_i is assigned to a subdomain D_i. Right: data-decomposition. Each processor P_i is assigned to a block $\mathcal{A}_i$ of data (i.e. a subset of rays) for the whole spatial domain D. Each block $\mathcal{A}_i$ is partitioned into $\mathcal{T}$ tiles. The tiling is illustrated by means of dashed lines for $\mathcal{T} = 2$. The two decompositions correspond to the coupling induced by Σ and Λ respectively, which can be applied without communication on the two partitions.

6.1. Spectral line and atmospheric model

We consider the Ca I line at 4227 Å, an ideal test case for new approaches to the non-LTE RT modeling of scattering polarization including PRD effects. Indeed, this line can be suitably modeled by considering a simple two-level atomic model, and it shows a clear scattering polarization signal, with a peculiar triplet-peak structure produced by PRD effects [e.g., 17,81,16]. We consider the frequency interval corresponding to the wavelength interval $[\lambda_{\min}, \lambda_{\max}] = [4226.2, 4227.2]$ Å, discretized with $N_\nu = 64$ nodes.

As a model of the solar atmosphere, we consider model C of [82] (hereafter, FAL-C). In particular, we consider the atmospheric height interval $[z_{\min}, z_{\max}] = [-100, 2210]$ km, discretized with $N_z = 64$ nodes. In the x and y directions we use an equidistant grid with $N_x = N_y$, $x_{\min} = y_{\min} = 0$, $x_{\max} = y_{\max}$, and $\Delta x = \Delta y = x_{\max}/N_x$. Case by case, the full list of dimensions can be found in tables and figures captions. If not specified, no magnetic and bulk velocity fields are included in the calculations. Regarding data decomposition, we used a single tile, i.e. $\mathcal{T} = 1$.

The population of the lower level (i.e., the ground level of neutral calcium) is calculated with the 1D module of the RH code [37], considering an atomic model composed of 25 levels (including 5 levels of Ca II and the ground level of Ca III), and taking AD PRD effects into account.

6.2. Validation and physical insights

For validation, we consider a 3D plane-parallel setting where the FAL-C atmospheric parameters and the population of the lower level are constant w.r.t. x and y. In this case, we obtain the same Stokes profiles as in the 1D FAL-C model[10] (e.g., see the red solid profile and blue circles in Fig. 5 for Q/I). Due to the cylindrical symmetry and to the absence of magnetic fields, Stokes U/I (see blue dashed profile in Fig. 5) and V/I are zero. Moreover, the profiles coincide with those obtained in previous 1D investigations [16,36]. The agreement is equally good for non-zero magnetic fields and/or bulk velocities, thus no plot is shown.

The robustness of the proposed iterative strategy to more complex atmospheric models is tested by considering a sinusoidal temperature

$$T_c = T_{\text{FAL-C}}(z)(1 + \cos(2\pi x/x_{\max})\cos(2\pi y/y_{\max})/2),$$

resulting in the same convergence behaviour as in the plane parallel case. Crucially, the breaking of the cylindrical symmetry induced by the horizontal variations of the temperature gives rise to a non-zero U/I polarization signal also in the absence of magnetic fields (green dashed profile in Fig. 5). Notably, the sign of U/I changes depending on the considered line of sight (see U/I panel in the upper row of Fig. 6).

In Fig. 6 polarization profiles with and without magnetic fields are presented. As expected, the presence of a non-zero magnetic field influences the polarization signals Q/I, U/I, and V/I, but not the intensity profile. The variation of the Q/I and U/I signals in the line-core region is due to the Hanle effect, while the variation of the wing lobes is due to the magneto-optical effects. The V/I signal is instead produced by the Zeeman effect.

[10] The 1D solution is obtained with the 1D code developed in [36], which implements the same formal solver and iterative strategy of the present study.

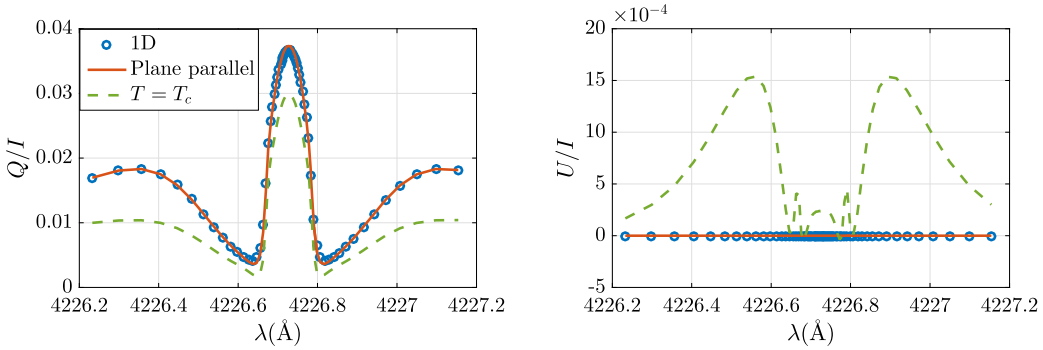

Fig. 5. Emergent fractional linear polarization profiles Q/I (left) and U/I (right) at $\boldsymbol{r} = (0, 0, z_{\max})$ for $\boldsymbol{\Omega} = (1.40, 0.39)$. We consider a 1D FAL-C model, a 3D plane-parallel FAL-C model, and the same 3D model but with temperature T_c. A setting with $N_x = N_y = N_\chi = 8$, $N_\theta = 12$, $N_z = N_\nu = 64$, and $\Delta x = \Delta y = 100$ km is used. The reference direction for positive Stokes Q is parallel to the $x - y$ plane. Four PGMRES iterations are needed to converge in all cases.

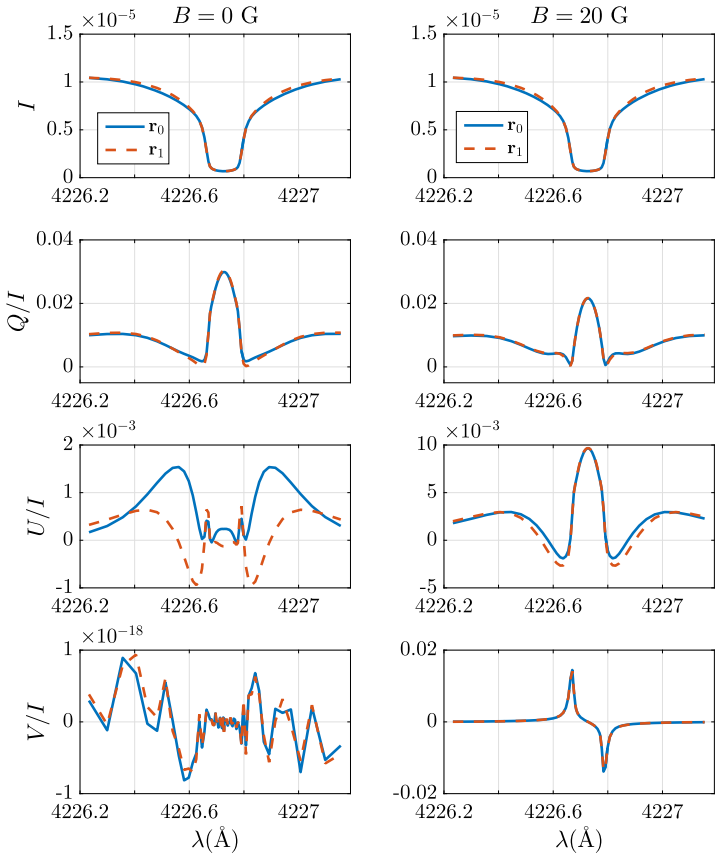

Fig. 6. Intensity and fractional polarization signals of the radiation emergent at $\boldsymbol{r}_0 = (0, 0, z_{\max})$ and $\boldsymbol{r}_1 = (200, 200, z_{\max})$, with $\boldsymbol{\Omega} = (1.40, 0.39)$. A setting with $N_x = N_y = N_\chi = 8$, $N_\theta = 12$, $N_z = N_\nu = 64$, $\Delta x = \Delta y = 100$ km, and $T = T_c$ is considered. *Upper row*: profiles obtained without magnetic fields. *Lower row*: profiles obtained including a magnetic field of 20 Gauss with direction $\boldsymbol{\Omega}_B = (\pi/2, 0)$, uniform in all the atmosphere. The reference direction for positive Stokes Q is parallel to the $x - y$ plane.

6.3. Scaling

In scaling results the total run-time is decomposed in its main components: the evaluation of Σ, $\widetilde{\Sigma}$, and Λ. The evaluation of Λ is further decomposed into communication costs (`MPI_Alltoall()`) and numerics (ODEs solutions).

In Table 1 and Fig. 7, we present a strong scaling study for a problem with $N \simeq 67.1 \cdot 10^6$ total degrees of freedom. For $N_p = 4096$, a processor is assigned to each spatial node and ray $(\boldsymbol{\Omega}, \nu)$, i.e. $N_p = N_s = N_\theta N_\chi N_\nu$, the scaling limit. In Table 2 and Fig. 8 we present a larger strong scaling study with $N \simeq 1.61 \cdot 10^9$. As expected, for $N_p > N_\theta N_\chi N_\nu$ the formal solution

Table 1
Timings (s) for the solution of the discretized RT problem (18) with $N_x = N_y = N_\theta = N_\chi = 8$, $N_z = N_\nu = 64$, $N \simeq 67.1 \cdot 10^6$, and $\Delta x = \Delta y = 100$ km, varying the number of processors N_p. All presented runs required 4 PGMRES iterations to converge.

N_p	64	128	256	512	1024	4096
Total runtime	6924	3471	1748	901	452	122
PRD scattering (Σ)	5341	2678	1343	651	318	79.9
CRD scattering ($\widetilde{\Sigma}$)	989	494	247	113	55.7	14.1
Formal solution (Λ)	108	61.8	33.2	29.0	19.3	11.6
Λ: `MPI_Alltoall()`	63.7	40.5	22.2	21.2	15.4	10.8
Λ: ODEs solution	42.3	21.2	10.6	5.4	2.7	0.67

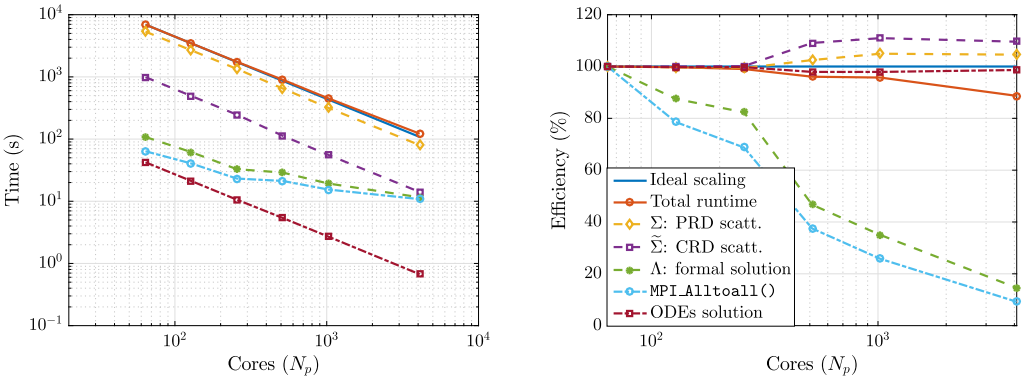

Fig. 7. Strong scaling and efficiency plots corresponding to Table 1.

Table 2
Run-times (s) for the solution of the discretized RT problem (18) with $N_x = N_y = 32$, $N_\theta = 12$, $N_\chi = 8$, $N_z = N_\nu = 64$, $N \simeq 1.61 \cdot 10^9$, and $\Delta x = \Delta y = 100$ km, varying the number of processors N_p. All presented runs required 4 PGMRES iterations to converge.

N_p	192	384	768	1536	3072	6144	12288
Total runtime			22002	10490	5240	2860	1576
PRD scattering (Σ)			17762	8418	4190	2248	1043
CRD scattering ($\widetilde{\Sigma}$)	6882	3404	1860	930	465	242	112
Formal solution (Λ)	1060	614	391	242	151	111	223
Λ: `MPI_Alltoall()`	725	446	298	186	129	93	186
Λ: ODEs solution	316	167	83.7	44.6	22.3	11.2	13.0

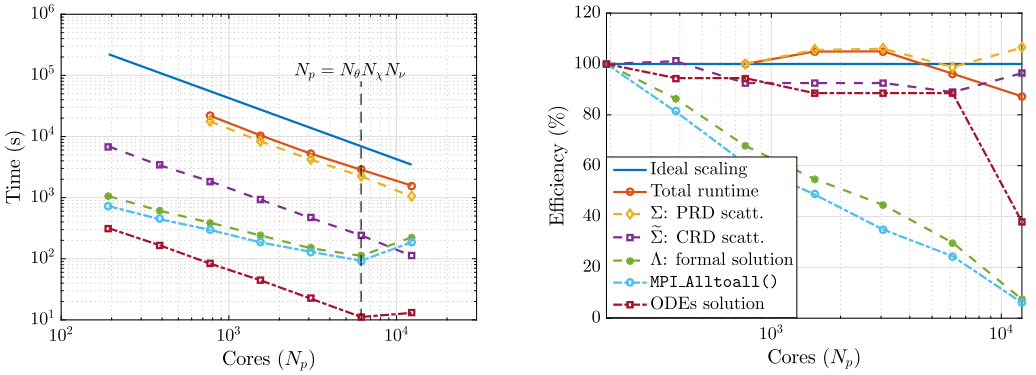

Fig. 8. Strong scaling and efficiency plots corresponding to Table 2.

is no longer scaling; on the other hand total runtime exhibits a near-optimal scaling since the computation of the emissivity remains the computational bottleneck.

Table 3
Runtimes (s) for the solution of the discretized RT problem (18) varying $N_x = N_y$ such that N/N_p is constant. We used $N_\theta = N_\chi = 8$ and $N_z = N_\nu = 64$. All presented runs required 4 PGMRES iterations to converge.

N_p	4	16	64	256	1024	4096
$N_x = N_y$	1	2	4	8	16	32
N	$1.6 \cdot 10^6$	$6.3 \cdot 10^6$	$2.5 \cdot 10^7$	$1.0 \cdot 10^8$	$4.0 \cdot 10^8$	$1.6 \cdot 10^9$
Total runtime	1341	1613	1693	1670	1788	1795
PRD scattering (Σ)	1115	1265	1361	1356	1302	1266
CRD scattering ($\widetilde{\Sigma}$)	173	219	216	220	220	220
Formal solution (Λ)	11.6	27.0	46.3	55.9	57.9	100
Λ: `MPI_Alltoall()`	3.9	15.4	34.7	44.4	42.5	81.1
Λ: ODEs solution	7.7	9.7	9.7	9.7	9.7	15.4

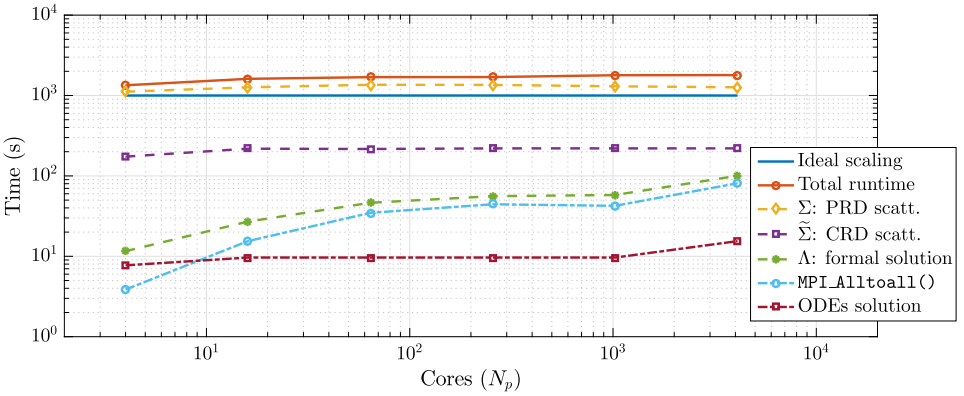

Fig. 9. Weak scaling plots corresponding to Table 3.

In Table 3 and Fig. 9 we present a weak scaling study with constant N/N_p ratio with $x_{\max} = y_{\max} = 1000$ km. We remark that an optimal weak scaling is crucial to tackle problems with finer spatial discretizations, e.g. with $N_x N_y N_z > 10^6$.

7. Conclusions

One of the main priorities in solar physics research is the development of novel diagnostic techniques for investigating the ever elusive magnetic fields of the outer layers of the solar atmosphere. In this context, a key step is to model the linear and circular polarization of strong resonance lines in state-of-the-art 3D models of the solar atmosphere, taking into account PRD effects, as well as the impact of arbitrary magnetic fields and bulk velocities. In this work, we presented a scalable solution strategy for the 3D non-LTE RT problem for polarized radiation in anisotropic and heterogeneous media, linearized as discussed in Section 2.3. The inclusion of PRD effects in the general AD setting and the high dimensionality of this vectorial RT problem make it computationally challenging. We employed well-studied discretization techniques for RT and a state-of-art iterative solution strategy, based on a physics-based preconditioner solving for a simpler scattering model (i.e., the CRD limit), to get a highly accurate solution in four iterations. A complete matrix-free approach made the implementation relatively lightweight, making a 3D RT simulation of scattering polarization with AD PRD effects possible, for the first time in the literature.

We presented numerical experiments for a two-level atom in a heterogeneous atmospheric model (based on FAL-C), possibly in the presence of arbitrary magnetic and bulk velocity fields. Experiments show a parallel efficiency close to 90%, up to the theoretical scaling limit (i.e. $N_p = N_s = N_\theta N_\chi N_\nu$). Full parallelism both in the spatial domain (for the computation of the emissivity) and in the ray propagation algorithm (for the formal solution) is obtained using two complementary decompositions. This strategy results in a simple implementation of the parallel ray propagation, with a single `MPI_Alltoall()` for every iteration and no need of ghost layers. Note that this decomposition approach requires the entirety of the data to be rearranged, hence its performance is bounded by the network bandwidth. Consequently, the `MPI_Alltoall()` call is the bottleneck for the formal solution computation, and tuning might become beneficial for larger scale runs. Nevertheless, its cost is negligible w.r.t. the total runtime, which is dominated by the computation of emissivity. Finally, we show how highly accurate 3D simulations of intensity and polarization profiles, accounting for PRD effects, with more than one billion of degrees of freedom, can be obtained on massively parallel machines in less than 30 minutes. We remark that the auxiliary grid decomposition currently limits memory scalability (for $N_p > N_\theta N_\chi N_\nu$) and therefore the spatial resolution of the problem. An additional spatial decomposition of the auxiliary grid and the use of MPI sub-communicators (avoiding the `MPI_Alltoall()` call) would lead to better scaling, both in terms of computing and memory, making it possible to

consider larger problems. Applications for realistic atmospheric models (with more than 10^{10} degrees of freedom), obtained from radiation magnetohydrodynamic simulations, will be the object of forthcoming studies.

We remark that the presented approach can be extended without significant difficulties to more complex atomic models for which the statistical equilibrium equations have an analytic solution and the problem can thus be linearized. One example is the case of a two-term atom with unpolarized lower term, which would allow modeling scattering polarization in various lines of high interest for investigating the solar chromosphere (e.g., Mg II h and k). In order to consider multi-level atomic systems, for which the statistical equilibrium equations need to be solved numerically, it is instead necessary to extend the approach to a non-linear setting. This would also be feasible but would require developing and testing non-linear solution strategies and it is foreseen as future research.

CRediT authorship contribution statement

Pietro Benedusi: Conceptualization, Investigation, Methodology, Software, Validation, Visualization, Writing – original draft, Writing – review & editing. **Simone Riva:** Investigation, Methodology, Software, Validation, Writing – original draft. **Patrick Zulian:** Software, Writing – review & editing. **Luca Belluzzi:** Conceptualization, Funding acquisition, Project administration, Supervision, Writing – original draft, Writing – review & editing. **Rolf Krause:** Funding acquisition, Project administration, Resources, Supervision, Writing – review & editing.

Declaration of competing interest

The authors declare that they have no known competing financial interests or personal relationships that could have appeared to influence the work reported in this paper.

Data availability

Data will be made available on request.

Acknowledgements

This work was financially supported by the Swiss National Science Foundation (SNSF) through grant CRSII5_180238. This project has received funding from the European High-Performance Computing Joint Undertaking (JU) under grant agreement No 955701. The JU receives support from the European Union's Horizon 2020 research and innovation program and Belgium, France, Germany, and Switzerland. Jiří Štěpán acknowledges the financial support of the grant 19-20632S of the Czech Grant Foundation (GAČR) and the support from project RVO:67985815 of the Astronomical Institute of the Czech Academy of Sciences. The authors wish to thank the anonymous referees for insightful comments that helped to improve the manuscript. Special thanks are extended to Gioele Janett and Javier Trujillo Bueno for their enriching comments on this work.

References

[1] S. Chandrasekhar, Radiative Transfer, Dover Publications, 1960.
[2] G.B. Rybicki, A.P. Lightman, Radiative Processes in Astrophysics, John Wiley & Sons, Inc., 1986.
[3] I. Hubeny, D. Mihalas, Theory of Stellar Atmospheres, Princeton University Press, 2014.
[4] M.F. Modest, Radiative Heat Transfer, Academic Press, 2013.
[5] K.F. Evans, The spherical harmonics discrete ordinate method for three-dimensional atmospheric radiative transfer, J. Atmos. Sci. 55 (3) (1998) 429–446.
[6] J. Trujillo Bueno, Polarized radiation observables for probing the magnetism of the outer solar atmosphere, in: K.N. Nagendra, J.O. Stenflo, Z.Q. Qu, M. Sampoorna (Eds.), Solar Polarization 7, in: Astronomical Society of the Pacific Conference Series, vol. 489, 2014, p. 137.
[7] J. Trujillo Bueno, E. Landi Degl'Innocenti, L. Belluzzi, The physics and diagnostic potential of ultraviolet spectropolarimetry, Space Sci. Rev. 210 (1) (2017) 183–226.
[8] J. Trujillo Bueno, J. Štěpán, L. Belluzzi, A. Asensio Ramos, R. Manso Sainz, T. del Pino Alemán, R. Casini, R. Ishikawa, R. Kano, A. Winebarger, F. Auchère, N. Narukage, K. Kobayashi, T. Bando, Y. Katsukawa, M. Kubo, S. Ishikawa, G. Giono, H. Hara, Y. Suematsu, T. Shimizu, T. Sakao, S. Tsuneta, K. Ichimoto, J. Cirtain, P. Champey, B. De Pontieu, M. Carlsson, CLASP constraints on the magnetization and geometrical complexity of the chromosphere-corona transition region, Astrophys. J. Lett. 866 (1) (2018) L15, https://doi.org/10.3847/2041-8213/aae25a, arXiv:1809.08865.
[9] R. Ishikawa, J.T. Bueno, T. del Pino Alemán, T.J. Okamoto, D.E. McKenzie, F. Auchère, R. Kano, D. Song, M. Yoshida, L.A. Rachmeler, K. Kobayashi, H. Hara, M. Kubo, N. Narukage, T. Sakao, T. Shimizu, Y. Suematsu, C. Bethge, B. De Pontieu, A.S. Dalda, G.D. Vigil, A. Winebarger, E.A. Ballester, L. Belluzzi, J. Štěpán, A.A. Ramos, M. Carlsson, J. Leenaarts, Mapping solar magnetic fields from the photosphere to the base of the corona, Sci. Adv. 7 (8) (2021) eabe8406, https://doi.org/10.1126/sciadv.abe8406, arXiv:2103.01583.
[10] R. Kano, J. Trujillo Bueno, A. Winebarger, F. Auchère, N. Narukage, R. Ishikawa, K. Kobayashi, T. Bando, Y. Katsukawa, M. Kubo, S. Ishikawa, G. Giono, H. Hara, Y. Suematsu, T. Shimizu, T. Sakao, S. Tsuneta, K. Ichimoto, M. Goto, L. Belluzzi, J. Štěpán, A. Asensio Ramos, R. Manso Sainz, P. Champey, J. Cirtain, B. De Pontieu, R. Casini, M. Carlsson, Discovery of scattering polarization in the hydrogen Lyα line of the solar disk radiation, Astrophys. J. Lett. 839 (1) (2017) L10, https://doi.org/10.3847/2041-8213/aa697f, arXiv:1704.03228.
[11] L.A. Rachmeler, J.T. Bueno, D.E. McKenzie, R. Ishikawa, F. Auchère, K. Kobayashi, R. Kano, T.J. Okamoto, C.W. Bethge, D. Song, E.A. Ballester, L. Belluzzi, T. d. Pino Alemán, A.A. Ramos, M. Yoshida, T. Shimizu, A. Winebarger, A.R. Kobelski, G.D. Vigil, B.D. Pontieu, N. Narukage, M. Kubo, T. Sakao, H. Hara, Y. Suematsu, J. Štěpán, M. Carlsson, J. Leenaarts, Quiet sun center to limb variation of the linear polarization observed by CLASP2 across the Mg II h and k lines, Astrophys. J. Lett. 936 (1) (2022) 67, https://doi.org/10.3847/1538-4357/ac83b8, arXiv:2207.01788.
[12] L. Belluzzi, J. Trujillo Bueno, J. Štěpán, The scattering polarization of the Lyα lines of H I and He II taking into account partial frequency redistribution and J-state interference effects, Astrophys. J. Lett. 755 (1) (2012), https://doi.org/10.1088/2041-8205/755/1/L2, arXiv:1207.0415.

[13] J. Štěpán, J. Trujillo Bueno, J. Leenaarts, M. Carlsson, Three-dimensional radiative transfer simulations of the scattering polarization of the hydrogen Lyα line in a magnetohydrodynamic model of the chromosphere-corona transition region, Astrophys. J. Lett. 803 (2) (2015) 65, https://doi.org/10.1088/0004-637X/803/2/65, arXiv:1501.06382.
[14] T. del Pino Alemán, J. Trujillo Bueno, R. Casini, R. Manso Sainz, The magnetic sensitivity of the resonance and subordinate lines of Mg II in the solar chromosphere, Astrophys. J. Lett. 891 (1) (2020) 91, https://doi.org/10.3847/1538-4357/ab6bc9.
[15] E. Alsina Ballester, L. Belluzzi, J. Trujillo Bueno, Solving the paradox of the solar sodium D_1 line polarization, Phys. Rev. Lett. 127 (8) (2021) 081101, https://doi.org/10.1103/PhysRevLett.127.081101, arXiv:2108.08334.
[16] G. Janett, E.A. Ballester, N. Guerreiro, S. Riva, L. Belluzzi, T. del Pino Alemán, J.T. Bueno, Modeling the scattering polarization of the solar Ca I 4227 Å line with angle-dependent partial frequency redistribution, A & A 655 (2021) A13, https://doi.org/10.1051/0004-6361/202141549, arXiv:2110.11990.
[17] M. Faurobert-Scholl, Hanle effect with partial frequency redistribution. II - linear polarization of the solar CA I 4227 A line, A & A 258 (2) (1992) 521–534.
[18] R. Holzreuter, D.M. Fluri, J.O. Stenflo, Scattering polarization in strong chromospheric lines. I. Explanation of the triplet peak structure, A & A 434 (2) (2005) 713–724, https://doi.org/10.1051/0004-6361:20042096.
[19] L. Belluzzi, J. Trujillo Bueno, The polarization of the solar Mg II h and k lines, Astrophys. J. Lett. 750 (1) (2012) L11, https://doi.org/10.1088/2041-8205/750/1/L11, arXiv:1203.4351.
[20] H.D. Supriya, H.N. Smitha, K.N. Nagendra, J.O. Stenflo, M. Bianda, R. Ramelli, B. Ravindra, L.S. Anusha, Center-to-limb observations and modeling of the Ca I 4227 å line, Astrophys. J. Lett. 793 (1) (2014) 42, https://doi.org/10.1088/0004-637X/793/1/42, arXiv:1407.5461.
[21] D.G. Hummer, Non-coherent scattering: I. The redistribution function with Doppler broadening, Mon. Not. R. Astron. Soc. 125 (1962) 21–37, https://doi.org/10.1093/mnras/125.1.21.
[22] V. Bommier, Master equation theory applied to the redistribution of polarized radiation in the weak radiation field limit. II. Arbitrary magnetic field case, A & A 328 (1997) 726–751.
[23] R. Casini, M. Landi Degl'Innocenti, R. Manso Sainz, E. Land i Degl'Innocenti, M. Landolfi, Frequency redistribution function for the polarized two-term atom, Astrophys. J. Lett. 791 (2) (2014) 94, https://doi.org/10.1088/0004-637X/791/2/94, arXiv:1406.6129.
[24] D.E. Rees, G.J. Saliba, Non-LTE resonance line polarization with partial redistribution effects, A & A 115 (1) (1982) 1–7.
[25] L. Anusha, K. Nagendra, Polarized line formation in multi-dimensional media. v. Effects of angle-dependent partial frequency redistribution, Astrophys. J. 746 (1) (2012) 84.
[26] M. Sampoorna, K.N. Nagendra, J.O. Stenflo, Polarized line formation in arbitrary strength magnetic fields angle-averaged and angle-dependent partial frequency redistribution, Astrophys. J. Lett. 844 (2) (2017) 97, https://doi.org/10.3847/1538-4357/aa7a15.
[27] L.S. Anusha, K.N. Nagendra, Polarized line formation in multi-dimensional media. IV. A Fourier decomposition technique to formulate the transfer equation with angle-dependent partial frequency redistribution, Astrophys. J. Lett. 739 (1) (2011) 40, https://doi.org/10.1088/0004-637X/739/1/40, arXiv:1308.3447.
[28] J. Štěpán, J. Trujillo Bueno, PORTA: a three-dimensional multilevel radiative transfer code for modeling the intensity and polarization of spectral lines with massively parallel computers, A & A 557 (2013) A143, https://doi.org/10.1051/0004-6361/201321742, arXiv:1307.4217.
[29] M. Badri, P. Jolivet, B. Rousseau, Y. Favennec, High performance computation of radiative transfer equation using the finite element method, J. Comput. Phys. 360 (2018) 74–92.
[30] E. Landi Degl'Innocenti, M. Landolfi, Polarization in Spectral Lines, Astrophysics and Space Science Library, vol. 307, Kluwer Academic Publishers, Dordrecht, 2004.
[31] J.C. Allred, A.F. Kowalski, M. Carlsson, A unified computational model for solar and stellar flares, Astrophys. J. Lett. 809 (1) (2015) 104, https://doi.org/10.1088/0004-637X/809/1/104, arXiv:1507.04375.
[32] E. Alsina Ballester, L. Belluzzi, J. Trujillo Bueno, The transfer of resonance line polarization with partial frequency redistribution in the general Hanle-Zeeman regime, Astrophys. J. Lett. 836 (2017) 6, https://doi.org/10.3847/1538-4357/836/1/6, arXiv:1609.05723.
[33] D. Mihalas, Stellar Atmospheres, 2nd edition, W.H. Freeman and Company, San Francisco, 1978.
[34] R. Casini, E. Landi Degl'Innocenti, Astrophysical plasmas, vol. 44, in: Fujimoto, Takashi, Atsushi Iwamae (Eds.), 2008, p. 247.
[35] T. del Pino Alemán, J. Trujillo Bueno, J. Štěpán, N. Shchukina, A novel investigation of the small-scale magnetic activity of the quiet sun via the hanle effect in the Sr I 4607 å line, Astrophys. J. Lett. 863 (2) (2018) 164, https://doi.org/10.3847/1538-4357/aaceab, arXiv:1806.07293.
[36] P. Benedusi, G. Janett, S. Riva, R. Krause, L. Belluzzi, Numerical solutions to linear transfer problems of polarized radiation III. Parallel preconditioned Krylov solver tailored for modeling PRD effects, A & A 664 (2022) A197.
[37] H. Uitenbroek, Multilevel radiative transfer with partial frequency redistribution, Astrophys. J. Lett. 557 (1) (2001) 389–398, https://doi.org/10.1086/321659.
[38] G. Janett, P. Benedusi, L. Belluzzi, R. Krause, Numerical solutions to linear transfer problems of polarized radiation. I. Algebraic formulation and stationary iterative methods, A & A 655 (2021) A87, https://doi.org/10.1051/0004-6361/202141237, arXiv:2110.11861.
[39] P. Benedusi, G. Janett, L. Belluzzi, R. Krause, Numerical solutions to linear transfer problems of polarized radiation. II. Krylov and matrix-free methods, A & A (2021), arXiv:1803.10945.
[40] M. Carlsson, V.H. Hansteen, B.V. Gudiksen, J. Leenaarts, B. De Pontieu, A publicly available simulation of an enhanced network region of the sun, A & A 585 (2016) A4, https://doi.org/10.1051/0004-6361/201527226, arXiv:1510.07581.
[41] M. Krook, On the solution of equations of transfer. I, Astrophys. J. Lett. 122 (1955) 488.
[42] S. Chandrasekhar, Radiative transfer, 1950.
[43] J. Štěpán, J. Jaume Bestard, J. Trujillo Bueno, Near optimal angular quadratures for polarised radiative transfer, A & A 636 (2020) A24, https://doi.org/10.1051/0004-6361/202037566, arXiv:2002.12736.
[44] J. Jaume Bestard, J. Štěpán, J. Trujillo Bueno, Improved near optimal angular quadratures for polarised radiative transfer in 3D MHD models, A & A 645 (2021) A101, https://doi.org/10.1051/0004-6361/202039424, arXiv:2012.04981.
[45] J. Reddy, V. Murty, Finite-element solution of integral equations arising in radiative heat transfer and laminar boundary-layer theory, numerical heat transfer, part B: fundamentals 1, Numer. Heat Transf., Part B, Fundam. 1 (3) (1978) 389–401.
[46] P.J. Coelho, Advances in the discrete ordinates and finite volume methods for the solution of radiative heat transfer problems in participating media, J. Quant. Spectrosc. Radiat. Transf. 145 (2014) 121–146, https://doi.org/10.1016/j.jqsrt.2014.04.021.
[47] D. Balsara, Fast and accurate discrete ordinates methods for multidimensional radiative transfer. Part I, basic methods, J. Quant. Spectrosc. Radiat. Transf. 69 (6) (2001) 671–707.
[48] D. Le Hardy, Y. Favennec, B. Rousseau, Solution of the 2-D steady-state radiative transfer equation in participating media with specular reflections using SUPG and DG finite elements, J. Quant. Spectrosc. Radiat. Transf. 179 (2016) 149–164.
[49] J. Kópházi, D. Lathouwers, A space-angle DGFEM approach for the Boltzmann radiation transport equation with local angular refinement, J. Comput. Phys. 297 (2015) 637–668.
[50] P.J. Coelho, A hybrid finite volume/finite element discretization method for the solution of the radiative heat transfer equation, J. Quant. Spectrosc. Radiat. Transf. 93 (1–3) (2005) 89–101, https://doi.org/10.1016/j.jqsrt.2004.08.014.
[51] J.-L. Guermond, G. Kanschat, J.C. Ragusa, Discontinuous Galerkin for the radiative transport equation, in: Recent Developments in Discontinuous Galerkin Finite Element Methods for Partial Differential Equations, Springer, 2014, pp. 181–193.

[52] M.M. Crockatt, A.J. Christlieb, C.D. Hauck, Improvements to a class of hybrid methods for radiation transport: Nyström reconstruction and defect correction methods, J. Comput. Phys. 422 (2020) 109765.
[53] V. Heningburg, C.D. Hauck, A hybrid finite-volume, discontinuous Galerkin discretization for the radiative transport equation, Multiscale Model. Simul. 19 (1) (2021) 1–24.
[54] L. Stenholm, H. Störzer, R. Wehrse, An efficient method for the solution of 3-D radiative transfer problems, J. Quant. Spectrosc. Radiat. Transf. 45 (1) (1991) 47–56.
[55] A. Wittmann, Computation and observation of Zeeman multiplet polarization in Fraunhofer lines, Sol. Phys. 35 (1) (1974) 11–29.
[56] P. Kunasz, L.H. Auer, Short characteristic integration of radiative transfer problems: formal solution in two-dimensional slabs, J. Quant. Spectrosc. Radiat. Transf. 39 (1) (1988) 67–79.
[57] G. Guderley, C.-C. Hsu, A predictor-corrector method for a certain class of stiff differential equations, Math. Comput. 26 (1972) 51–69, https://doi.org/10.1090/S0025-5718-1972-0298952-7.
[58] D. Rees, G. Murphy, C. Durrant, Stokes profile analysis and vector magnetic fields. II-Formal numerical solutions of the Stokes transfer equations, Astrophys. J. Lett. 339 (1989) 1093–1106.
[59] G. Janett, E.S. Carlin, O. Steiner, L. Belluzzi, Formal solutions for polarized radiative transfer. I. The DELO family, Astrophys. J. Lett. 840 (2) (2017) 107.
[60] G. Janett, O. Steiner, L. Belluzzi, Formal solutions for polarized radiative transfer. II. High-order methods, Astrophys. J. Lett. 845 (2) (2017) 104.
[61] G. Janett, A. Paganini, Formal solutions for polarized radiative transfer. III. Stiffness and instability, Astrophys. J. Lett. 857 (2) (2018) 91.
[62] G. Janett, O. Steiner, L. Belluzzi, Formal solutions for polarized radiative transfer. IV. Numerical performances in practical problems, Astrophys. J. Lett. 865 (1) (2018) 16, https://doi.org/10.3847/1538-4357/aad4a4, arXiv:1809.06604.
[63] J. Trujillo Bueno, R. Manso Sainz, Iterative methods for the non-LTE transfer of polarized radiation: resonance line polarization in one-dimensional atmospheres, Astrophys. J. Lett. 516 (1) (1999) 436–450, https://doi.org/10.1086/307107.
[64] I. Hubeny, Accelerated lambda iteration: an overview, in: Stellar Atmosphere Modeling, vol. 288, 2003, p. 17.
[65] E.W. Larsen, Unconditionally stable diffusion-synthetic acceleration methods for the slab geometry discrete ordinates equations. Part I: theory, Nucl. Sci. Eng. 82 (1) (1982) 47–63.
[66] P. Fabiani Bendicho, J. Trujillo Bueno, L. Auer, Multidimensional radiative transfer with multilevel atoms. II. The non-linear multigrid method, A & A 324 (1997) 161–176.
[67] B.W. Patton, J.P. Holloway, Application of preconditioned GMRES to the numerical solution of the neutron transport equation, Ann. Nucl. Energy 29 (2) (2002) 109–136.
[68] J. Warsa, K. Thompson, J. Morel, Improving the efficiency of simple parallel S_N algorithms with Krylov iterative methods, Trans. Am. Nucl. Soc. (2003) 449–451.
[69] L. Anusha, K. Nagendra, F. Paletou, L. Léger, Preconditioned bi-conjugate gradient method for radiative transfer in spherical media, Astrophys. J. Lett. 704 (1) (2009) 661.
[70] L. Anusha, K. Nagendra, F. Paletou, Polarized line formation in multi-dimensional media. ii. A fast method to solve problems with partial frequency redistribution, Astrophys. J. 726 (2) (2010) 96.
[71] K. Ren, R. Zhang, Y. Zhong, A fast algorithm for radiative transport in isotropic media, J. Comput. Phys. 399 (2019) 108958.
[72] M. Badri, P. Jolivet, B. Rousseau, Y. Favennec, Preconditioned Krylov subspace methods for solving radiative transfer problems with scattering and reflection, Comput. Math. Appl. 77 (6) (2019) 1453–1465.
[73] P. Jolivet, M.A. Badri, Y. Favennec, Deterministic radiative transfer equation solver on unstructured tetrahedral meshes: efficient assembly and preconditioning, J. Comput. Phys. 437 (2021) 110313.
[74] M.P. Adams, M.L. Adams, W.D. Hawkins, T. Smith, L. Rauchwerger, N.M. Amato, T.S. Bailey, R.D. Falgout, Provably optimal parallel transport sweeps on regular grids, Tech. Rep., Lawrence Livermore National Lab. (LLNL), Livermore, CA (United States), 2013.
[75] T.M. Evans, A.S. Stafford, R.N. Slaybaugh, K.T. Clarno, Denovo: a new three-dimensional parallel discrete ordinates code in scale, Nucl. Technol. 171 (2) (2010) 171–200.
[76] S.D. Pautz, T.S. Bailey, Parallel deterministic transport sweeps of structured and unstructured meshes with overloaded mesh decompositions, Nucl. Sci. Eng. 185 (1) (2017) 70–77.
[77] S. Balay, S. Abhyankar, M.F. Adams, J. Brown, P. Brune, K. Buschelman, L. Dalcin, V. Eijkhout, W.D. Gropp, D. Kaushik, M.G. Knepley, L.C. McInnes, K. Rupp, B.F. Smith, S. Zampini, H. Zhang, PETSc Web page, http://www.mcs.anl.gov/petsc, 2015, http://www.mcs.anl.gov/petsc.
[78] S. Balay, S. Abhyankar, M.F. Adams, J. Brown, P. Brune, K. Buschelman, L. Dalcin, V. Eijkhout, W.D. Gropp, D. Kaushik, M.G. Knepley, L.C. McInnes, K. Rupp, B.F. Smith, S. Zampini, H. Zhang, PETSc users manual, Tech. Rep. ANL-95/11 - Revision 3.6, Argonne National Laboratory, 2015, http://www.mcs.anl.gov/petsc.
[79] S. Balay, W.D. Gropp, L.C. McInnes, B.F. Smith, Efficient management of parallelism in object oriented numerical software libraries, in: E. Arge, A.M. Bruaset, H.P. Langtangen (Eds.), Modern Software Tools in Scientific Computing, Birkhäuser Press, 1997, pp. 163–202.
[80] P. Zulian, D. Ramelli, SGRID: a structured grid manager for supercomputing, https://bitbucket.org/zulianp/grid, 2020, https://bitbucket.org/zulianp/sgrid.
[81] E. Alsina Ballester, L. Belluzzi, J. Trujillo Bueno, Magneto-optical effects in the scattering polarization wings of the Ca I 4227 å resonance line, Astrophys. J. Lett. 854 (2) (2018) 150, https://doi.org/10.3847/1538-4357/aa978a, arXiv:1711.00372.
[82] J.M. Fontenla, E.H. Avrett, R. Loeser, Energy balance in the solar transition region. III - helium emission in hydrostatic, constant-abundance models with diffusion, Astrophys. J. Lett. 406 (1993) 319–345, https://doi.org/10.1086/172443.